Faculty of Physics and Astronomy
University of Heidelberg

Diploma thesis
in Physics

submitted by
Thomas Lompe
born in Nienburg
2008

An apparatus for the production of molecular Bose-Einstein condensates

This diploma thesis has been carried out by
Thomas Lompe at the
Max-Planck-Institute for Nuclear Physics
under the supervision of
Juniorprofessor Dr. S. Jochim

This thesis reports on the construction of an apparatus capable of producing a molecular Bose-Einstein-Condensate (BEC) of $^6\mathrm{Li}_2$.

To create a condensate fermionic lithium is first evaporated in an oven, slowed by a Zeeman slower and captured in a magneto-optical-trap (MOT). A scheme for creating time-averaged arbitrary optical potentials for optimized transfer of the atoms from the MOT to a high-power, far detuned optical dipole trap was implemented, as well as magnetic field coils to tune the interactions of the atoms via Feshbach resonances.

The first experiments with the new machine include the characterization of the optical dipole trap and evaporative cooling of $^6\mathrm{Li}$.

Diese Diplomarbeit beschreibt den Aufbau einer Apparatur zur Herstellung molekularer Bose-Einstein-Kondensate (BEC) aus $^6\mathrm{Li}_2$.

Die benötigten Lithiumatome werden in einem Ofen verdampft, von einem Zeemannslower abgebremst und in einer Magnetooptischen Falle (MOT) gefangen. Für den optimierten Transfer von der MOT in die mit großer Leistung betriebene Dipolfalle wurde ein System zur Erzeugung zeitgemittelter optischer Potentiale eingerichtet. Um die Wechselwirkung zwischen den Atomen kontrollieren wurden Spulen zur Erzeugung großer Magnetfelder entwickelt.

Zu den ersten Experimenten mit dem neuen Aufbau gehören die Charakterisierung der optischen Dipolfalle und das evaporative Kühlen von $^6\mathrm{Li}$.

Contents

1 Introduction **1**

2 Trapping and cooling of Lithium **5**
2.1 Trapping neutral atoms 5
2.1.1 Magneto-optical trap 6
2.1.2 Red-detuned dipole traps 6
2.2 Collisonal properties of ultracold gases 8
2.2.1 Elastic scattering 8
2.2.2 Feshbach Resonance and bound state 10
2.3 Evaporative cooling 15
2.3.1 Principles of evaporative cooling 15
2.3.2 Evaporation of atom-molecule mixtures 17
2.4 Key properties of BECs 17
2.4.1 Critical temperature and condensate fraction 18
2.4.2 Density distribution of a BEC in the ground state 19

3 Experimental Setup **21**
3.1 Vacuum system 21
3.2 671nm laser System 22
3.2.1 Frequency reference and offset locks 23
3.2.2 Magneto-optical trap 24
3.2.3 Imaging systems 27
3.3 Optical dipole trap 31
3.3.1 Setup of the crossed beam trap 32
3.3.2 Thermal lensing 33
3.3.3 Time-averaged dipole trapping 35
3.4 Feshbach coils 38
3.4.1 Coil design and technical challenges 38
3.4.2 Performance of the Feshbach coils 39
3.5 Experiment control 41

4 Evaporative cooling of Lithium **43**
4.1 Loading of the crossed dipole trap 43
4.1.1 Preparing the MOT for transfer 43
4.1.2 Adjusting the optical dipole trap 46
4.1.3 Transfer efficiency 47
4.1.4 First stage of forced evaporation 47
4.2 Tuning the interactions 50
4.3 Plain evaporation 51
4.4 Properties of the dipole trap 52
4.4.1 Lifetime measurements 52
4.4.2 Determining the trap frequencies 53
4.5 Starting conditions for forced evaporation 57

5 Conclusion and Outlook **59**

A Relevant transitions of ^{6}Li **61**

Bibliography **63**

Chapter 1

Introduction

Although Bose-Einstein condensation was predicted theoretically in 1925, it took 70 years until experimentalists provided convincing proof of this phenomenon. The reason was that the phase transition to a BEC occurs at a phase space density on the order of one, which can be understood as having an equal amount of particles and available quantum states in the system. In comparison, the phase space density of a normal gas at room temperature is roughly 10^{-11}, a difference which made this regime impossible to access experimentally for a long time.

The first success was the discovery of the superfluidity of $^4\mathrm{He}$ below a temperature of $2.17\,\mathrm{K}$, which can be explained by a model in which the superfluid is partly Bose-condensed. Yet the interactions in the liquid phase are so strong that the condensate fraction remains small and cannot be directly observed. These problems can be overcome by using dilute, weakly interacting samples, but to still reach high enough phase space densities the lower number density has to be compensated by a further decrease in temperature.

This became possible with the development of techniques for laser cooling and stable trapping of neutral atoms in the 1980s, finally leading to the creation of the first pure BECs in 1995 by Cornell, Wieman [1], Ketterle [2] and Hulet [3], who cooled gaseous samples with number densities of $n \sim 10^{14}\,\mathrm{cm}^{-3}$ to temperatures in the nanokelvin range.

To create the first BECs a two-stage process was used. The first step is to capture and cool atoms in a magneto-optical trap (MOT), where phase space densities on the order of 10^{-4} can be reached. This provides excellent starting conditions for the second stage, where the atoms are placed in a conservative potential. Particles carrying more than the average kinetic energy are then selectively removed from the sample, a process called evaporative cooling. This has since become the "standard" way to create BECs and is used by more than fifty research groups around the world.

There are several advantadges to such a dilute, ultracold system. One is that the

interactions in the system are weak and can be described by a single parameter, the s-wave scattering length a, which allows a consistent theoretical description. Another is the possibility to manipulate and directly probe the condensate by optical means. These advantages make BECs attractive both as model systems for condensed matter phenomena and to investigate fundamental questions of quantum mechanics.

BECs became an even more versatile tool with the discovery of Feshbach resonances in ultracold gases, which cause the scattering length to diverge to $\pm\infty$ [4]. These resonances can be accessed by simply applying a homogeneous magnetic field, which allows to easily tune the sign and strength of the interactions.

The same techniques can with some modifications be applied to fermions as well, and by evaporatively cooling ^{40}K Debbie Jin and her group created the first degenerate Fermi gas in 1999 [5]. If the scattering length of such a gas is tuned to small negative values, corresponding to a weak attractive interaction, it behaves analogous to an electron gas in a solid and can be described by the model developed by Bardeen, Cooper and Schrieffer for superconductivity in metals [6]. So studies of ultracold Fermi systems might help to gain a better understanding of superconductivity. At large positive scattering lengths stable molecules are formed that can be condensed into a BEC [7] [8] [9], which gives rise to the hope that ultracold chemistry could be performed on these or similar systems.

It is possible to continuosly move from one regime to the other through simple magnetic field ramps across a Feshbach resonance. This transition turned out to be completely reversible, a phenomenon which was predicted as the BEC-BCS crossover. Right on resonance lies the so called unitary regime, where the interactions only depend on the momentum of the particles and one universal parameter β. This has the amazing consequence that all Fermi systems in this regime behave the same. Some examples of strongly interacting Fermi systems include neutron stars or the quark-gluon plasma, and there are ideas to model these systems using ultracold gases.

Yet with our experiment we intend to use the advances made in the field of cold fermions to pursue a different goal. From a theoretical point of view, all the systems mentioned above are treated by applying quantum statistics to a Bose or Fermi gas. But statistical approaches are only valid for large ensembles. If the particle number is too small the approximation breaks down, and one has to use many-body-theory for a proper description. Such a system could then serve as a model for a completely different class of problems.

To do experiments with small fermionic systems, we will have to be able to reliably prepare them in the ground state, i.e. to have all states up to the Fermi energy occupied. This is hard to achieve by evaporative cooling of fermions, as in a Fermi gas close to zero temperature Pauli blocking forbids collisions except for atoms in a small region close to the fermi surface. But if we tune the interactions

to large positive values using a Feshbach resonance we have a system of bosonic molecules, in which we can create an almost pure BEC. Doing an adiabatic magnetic field ramp across the resonance should then give us a Fermi gas with a high occupation probability for the lowest-lying states. The final challenges will probably be to precisely control the number of remaining atoms, and to make sure that they are not heated by the spilling of the excess atoms from the trap.

Due to its broad Feshbach resonance, which allows for easy and precise tuning of the interactions, ^{6}Li is the obvious choice for this experiment. Thus the first step will be a molecular Bose-Einstein condensate of lithium, which was first realized in 2003 by the group of Rudi Grimm [7]. At the moment there are seven groups with $^6Li_2$ BECs; the physics are well understood and there is quite a lot of experience available. But as we want our BEC only as a starting point for experiments on small Fermi systems, our requirements differ somewhat from those of the other experiments. We do not expect to need BECs containing much more than 10^4 molecules, final temperature and the stability of the trap will be of far greater importance than the maximum number of particles in the BEC. Other critical aspects are reliability and low maintenance. We tried to achieve this by keeping the machine as simple as possible and using techniques and components known to work well wherever possible.

The one property for which we were willing to take chances was the repetition rate of the experiment, as we expect that a lot of trial and error will be necessary to achieve our goal.

Contents of this thesis

This thesis reports on the construction of our experimental apparatus. It consists of two main parts, the first being the following chapter in which a brief reminder of some key physical concepts important for the creation of a BEC will be given.

The second part starts by describing the experimental setup in chapter three, skipping the details of the vacuum setup and the MOT as those were discussed in an earlier thesis [10], focussing instead on the optical dipole trap and the coils providing homogenous offset fields to access the Feshbach resonance. In chapter four the properties of our dipole trap are investigated and the procedure for transfering the atoms from the MOT to the dipole trap is introduced. It closes with an account of our first attempts at evaporative cooling towards a BEC.

The final chapter sums up the progress made in the setup of the experiment since the founding of our group in October 2006 and gives a brief overview of the things that still need to be done on the way to experiments on mesoscopic fermionic systems.

Chapter 2

Trapping and cooling of Lithium

This chapter aims to give a brief describtion of the major aspects needed to understand the experimental setup and measurements which are adressed in chapters 3 and 4.

The chapter starts by describing the methods employed for trapping and cooling of atoms. We then investigate their collisonal behavior, the tunability of their elastic scattering, and how the change in the collisional behavior leads to a molecular bound state. Production processes and stability of these molecules are discussed, as well as the formation of a chemical equlibrium of atoms and molecules at low temperature. The evaporative cooling of such a mixture towards a BEC is addressed. A short discussion of the transition temperature T_c and the spatial distribution of a BEC in a trap closes the chapter.

2.1 Trapping neutral atoms

If one wants to do experiments with ultracold gases, the basic requirement and at the same time one of the great challenges is trapping the atoms. For this a wide variety of traps is used.

The first step in almost all experiments is the magneto-optical trap, which can trap atoms at room temperature and cool them down to temperatures ranging from one to several hundred μK, depending on the atomic species and the sophistication of the cooling techniques. In the case of Lithium it allows the preparation of a cold sample with $N \approx 10^9$ atoms at a temperature of $T_{\min} \approx 200\,\mu$K, with a phase space density on the order of 10^{-5}.

To further increase the phase space density to values above unity one needs to perform evaporative cooling, which requires a conservative potential, and can therefore not be performed in a MOT. Thus the sample is transferred into a different trap that fulfills this condition, which is usually a magnetic or optical dipole

trap.

2.1.1 Magneto-optical trap

As our MOT has already been investigated by Friedhelm Serwane, this section will only mention some properties of magneto-optical traps important for the transfer of the atoms to another trap and refer to his diploma thesis [10] for an in-depth analysis of our MOT. For further details on the principles of laser cooling see [11].

An atom moving with velocity v in two counterpropagating laser beams with wavenumbers $k = 2\pi/\lambda$ has a doppler shift $\Delta\omega = kv$. For near-resonant light this leads to a net force of

$$\langle F \rangle = \hbar k \gamma_1 - \hbar k \gamma_2 \tag{2.1}$$

due to the different rates $\gamma_{1,2}$ for photon scattering. It is called the spontaneous force and depends on the detuning δ of the lasers, the linewidth Γ of the transition and the saturation parameter s_0 of the laser beams. For small doppler shifts it can be written as

$$\langle F \rangle \cong \frac{8\hbar k^2 \delta_0 s_0}{\Gamma(1 + s_0 + (\frac{2\delta_0}{\Gamma})^2)^2} v \equiv -\beta v. \tag{2.2}$$

For red-detuned beams this force has a damping effect with a damping coefficent β, thus cooling the atom in what is called an optical molasses. At the same time a heating rate is introduced by the spontaneous emission of the absorbed photons, which is given by the scattering rate times the recoil energy $E_\mathrm{r} = \hbar^2 k^2 / 2m$. By equating cooling and heating rate one gets the temperature in the thermal equlibrium

$$k_B T = \frac{\hbar\Gamma}{4} \frac{1 + (2\delta/\Gamma)^2}{(|\delta|/\Gamma)}, \tag{2.3}$$

which becomes minimal for a detuning $\delta = -\Gamma/2$.

In an optical molasses the atoms are only cooled, not trapped. To achieve this a magnetic field gradient is applied along the laser beam, which lifts the degeneracy of the magnetic sublevels of the transition. By using circularly polarized light one can create a spatial dependence of the spontaneous force, which leads to a confinement of the atoms (see fig. 2.1).

2.1.2 Red-detuned dipole traps

In our experiment we use a red-detuned optical dipole trap to hold the atoms during evaporation. The principle behind this trap can be understood using a simple classical model [12]:

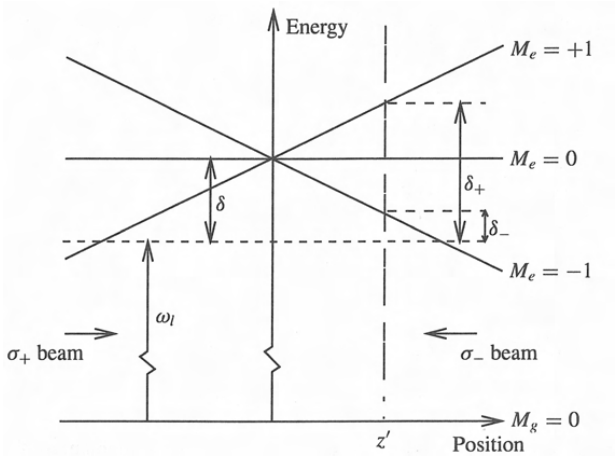

Figure 2.1: Schematic of a one-dimensional MOT. One can see that the confinement can be increased either by lowering the detuning or increasing the magnetic field gradient. Figure taken from [11].

The oscillating electric field of the laser

$$\mathbf{E}(\mathbf{r},t) = \hat{e}\,\tilde{E}\,(\mathbf{r})\,e^{-i\omega t} + c.c. \tag{2.4}$$

drives a forced oscillation of the atom, which results in an induced dipole moment

$$\mathbf{p}\,(\mathbf{r},t) = \hat{e}\,\tilde{p}\,(\mathbf{r})\,e^{-i\omega t} + c.c.. \tag{2.5}$$

The amplitude of the dipole moment can be expressed as

$$\tilde{p} = \alpha\,\tilde{E} \tag{2.6}$$

where $\alpha(\omega)$ is the complex polarizability of the atom. The real part of the polarizability leads to the interaction potential

$$U_{\text{dip}} = -\frac{1}{2}\,\langle \mathbf{pE} \rangle = -\frac{1}{2\epsilon_0 c}\,\text{Re}(\alpha)\,I \tag{2.7}$$

which results in the dipole force

$$\mathbf{F}_{\text{dip}}(\mathbf{r}) = -\nabla U_{\text{dip}}(\mathbf{r}), \tag{2.8}$$

so the dipole potential is conservative.

The imaginary part describes the absorbtion of power from the field through the oscillator

$$P_{\text{abs}} = \langle \dot{\mathbf{p}}\mathbf{E} \rangle = 2\omega\,\text{Im}(\tilde{p}\tilde{E}^*) = \frac{\omega}{\hbar\epsilon_0 c}\,\text{Im}(\alpha)\,I(\mathbf{r}) \tag{2.9}$$

which leads to scattering of photons at a rate of

$$\Gamma_{\mathrm{sc}}(\mathbf{r}) = \frac{P_{\mathrm{abs}}}{\hbar\omega}. \tag{2.10}$$

In the case of an alkali atom in a laser field detuned very far from the resonance, a condition which is very well fulfilled in our case, α can be approximated by the classical model of a forced, damped oscillator with an eigenfrequency corresponding to the optical dipole transition of the atom. This approximation leads to the following expressions for dipole potential the scattering rate, where ω_0 and ω are the angular frequencies of the resonance and the trapping light, and Γ is the linewidth of the resonant transition:

$$U_{\mathrm{dip}}(\mathbf{r}) = -\frac{3\pi c^2}{2\omega_0^3}\left(\frac{\Gamma}{\omega_0-\omega}+\frac{\Gamma}{\omega_0+\omega}\right) I(\mathbf{r}) \tag{2.11}$$

$$\Gamma_{\mathrm{sc}}(\mathbf{r}) = -\frac{3\pi c^2}{2\omega_0^3}\left(\frac{\omega}{\omega_0}\right)^3\left(\frac{\Gamma}{\omega_0-\omega}+\frac{\Gamma}{\omega_0+\omega}\right)^2 I(\mathbf{r}) \tag{2.12}$$

One can see from eqn. 2.11 that red-detuned light attracts an atom while blue-detuned light repels it, and that the strength of the force drops linearly with growing detuning. Equation 2.12 shows a fundamental disadvantage of optical dipole traps: Although the photons forming the trapping potential are non-resonant, there is still a probability for elastic collisions with the atoms. These processes lead either to heating or - especially in the later stages of the experiment, when the trap depth is comparable to the recoil energy - to losses of atoms from the trap. Fortunately the scattering rate scales with the square of the detuning, so it is possible to simultaneously achive a deep trapping potential and low heating rates, but at the price of large detuning and high laser power.

The consequences of this result for our trapping setup are discussed in section 3.3.

2.2 Collisonal properties of ultracold gases

2.2.1 Elastic scattering

The concept of the scattering length

Elastic quantum mechanical scattering in a radially symmetric potential can be described in the long-distance limit by the combination of an incident plane wave Φ_{inc} and an outgoing spherical wave Φ_{sc},

$$\Phi(\mathbf{r}) = \Phi_{\mathrm{inc}} + \Phi_{\mathrm{sc}} = e^{ikz} + f(\theta,k)\,\frac{e^{ikr}}{r} \tag{2.13}$$

where $f(\theta, k)$ is the probability amplitude for a particle of momentum $\hbar k$ to scatter under an angle θ. $f(\theta, k)$ is directly related to the differential cross section $\frac{d\sigma}{d\Omega}$ by

$$\frac{d\sigma}{d\Omega} = |f(\theta, k)|^2 . \tag{2.14}$$

Due to the rotational symmetry of the system, a separation of $\Phi(\mathbf{r})$ into an angular and radial component is possible. The angular component is expanded into the eigenfunctions of angular momentum, the Legendre polynominals $P_l(\cos\theta)$, which leads to

$$\Phi_{\mathrm{sc}}(\mathbf{r}) = \sum_{l=0}^{\infty} R_{\mathrm{l}}(r)\, P_l(\cos\theta). \tag{2.15}$$

Solving the radial Schrödinger equation for R_{l} gives for $r \to \infty$

$$R_{\mathrm{l}} = A_{\mathrm{l}} \frac{1}{kr} \sin\left(kr - \frac{\pi}{2}l + \delta_{\mathrm{l}}\right). \tag{2.16}$$

Here δ_{l} is the phase shift between the scattered and the unperturbed wave caused by the scattering potential; it contains all information relevant for the scattering process. By inserting 2.16 in 2.13 and expanding Φ_{inc} into spherical waves as well one can get the following expression for the scattering amplitude:

$$f(\theta, k) = \frac{1}{2ik} \sum_{l=0}^{\infty} (2l+1)\left(e^{2i\delta_{\mathrm{l}}} - 1\right) P_{\mathrm{l}}(\cos\theta) \tag{2.17}$$

Now one can integrate 2.14 to get the total cross section

$$\sigma(k) = \frac{4\pi}{k^2} \sum_{l=0}^{\infty} (2l+1)\, \sin^2\delta_{\mathrm{l}}. \tag{2.18}$$

As the centrifugal barrier causes the scattering phase to scale like $\delta_{\mathrm{l}} \propto k^{2l+1}$ if the momentum is small compared to the range of the interatomic potential r_0, scattering processes with $l > 0$ are suppressed for $k \ll \frac{1}{r_0}$, which is well fulfilled at ultracold temperatures. For the case of purely s-wave scattering with $l = 0$ we get the scattering amplitude

$$f_0 = \frac{1}{2ik}\left(e^{2i\delta_0} - 1\right). \tag{2.19}$$

By defining the scattering length a through

$$\lim_{k \ll 1/r_0} \frac{\tan\delta_0}{k} = -a \tag{2.20}$$

and using $\delta_0 \sim k$ we arrive at the final result for the scattering amplitude

$$f = -\frac{a}{1+ika}. \tag{2.21}$$

In a weakly interacting gas with $ka \ll 1$ this leads to a total elastic cross section of $\sigma = 4\pi a^2$ for two non-identical particles, which is independent of their momentum. For the strongly interacting case with $ka \gg 1$, a regime in which most of our experiments will take place, the scattering amplitude is limited by the momentum to $f = -\frac{1}{ik}$ and we get a cross section of $\sigma = \frac{4\pi}{k^2}$.

The details to this brief summary can be found in [13] and [14].

Resonantly enhanced scattering

The sign and the value of a depend critically on the shape and depth V of the scattering potential. Calculating the effects of changing depths on a simple box potential one finds the following:

For very shallow potentials, where no bound state exists, the scattering length is small and negative, corresponding to a weak attractive interaction.

If one increases the potential depth, in a regime close to critical depth V_c where a bound state forms, the size of the scattering length increases for $V \to V_\mathrm{c}$, which is due to the coupling of the incoming wavefunction with the quasi-bound state above the continuum. This phenomenon leads to the unusually large triplet scattering length of ^{6}Li mentioned below. For $V = V_\mathrm{c}$ the strength of this coupling becomes infinite, and the scattering length diverges to $a \to -\infty$ for $V \uparrow V_\mathrm{c}$. If $V > V_\mathrm{c}$ a true bound state exists, which leads to a positive value for the scattering length. The closer the state lies to the continuum, the larger a becomes, with $a \to +\infty$ for $V \downarrow V_\mathrm{c}$.

This phenomenon is called a scattering resonance and occurs every time a bound state lies close to the continuum.

2.2.2 Feshbach Resonance and bound state

Scattering channels

The interaction potential is given by the type and the internal state of the particles. We will refer to a set of quantum numbers fully describing the states of the colliding atoms as a channel.

In our experiment we prepare ^{6}Li atoms in a spin mixture of the two lowest-energy states $\left|F = \frac{1}{2}, m_\mathrm{F} = \pm\frac{1}{2}\right\rangle$, so we have to distinguish between the cases of antiparallel and parallel spin of the valence electron, which lead to singlet and triplet scattering with respective scattering lengths $a_\mathrm{s} \approx 39\,a_0$ and $a_\mathrm{tr} \approx -2240\,a_0$, where a_0 is Bohr's radius.

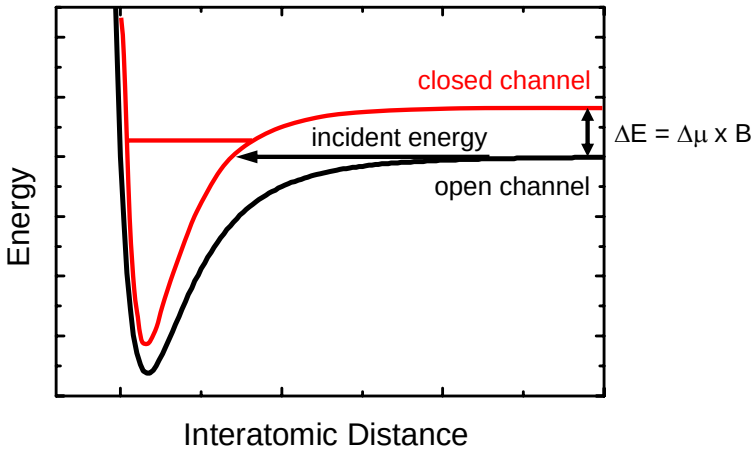

Figure 2.2: Schematic representation of the tuning of the scattering length in ^{6}Li: The total energy of the open (triplet) channel changes with $\Delta E = \Delta\mu B$, while the energy of the singlet state is unchanged. Therefore the continuum of the open channel can be brought to resonance with the bound state of the closed channel. Figure slightly adapted from [15]

In low magnetic fields $|m_\mathrm{s}\rangle$ is not a good quantum number, so the resulting scattering length is a linear combination of a_s and a_tr. Applying DC magnetic fields $B > 50\,\mathrm{G}$ causes the nuclear and electronic spin to decouple, and as $k_\mathrm{b}T \ll \mu_\mathrm{tr}B$ the sample becomes spin-polarized and scattering into the singlet state is forbidden. Therefore the triplet and singlet state can be referred to as the open and closed channel.

Feshbach basics

A Feshbach resonance is caused by second order coupling of an open to a closed channel. If the continuum of the open channel lies slightly below the total energy of the system in the bound state, particles scattered into the closed channel are in a virtual state; they have to return to the open channel after $\tau \approx \frac{\hbar}{E_\mathrm{bs}-E_\mathrm{cont}}$.

If $E_{\mathrm{cont}} > E_{\mathrm{bs}}$ they can enter the bound state, but for energy and momentum conservation to be fulfilled a third particle has to carry off the excess momentum. If this is not the case, both particles have to end up in the open channel again. Therefore one can understand that the resonant contribution to the scattering length has to scale with

$$a_{\mathrm{res}} \propto \frac{C}{E_{\mathrm{bs}} - E_{\mathrm{cont}}}. \tag{2.22}$$

To tune the scattering length one now just has to find a way to tune the difference in the total energy of the open and closed channel, thereby moving the position of the bound state relative to the continuum of the open channel. If the states have a difference $\Delta\mu = \mu_{\mathrm{open}} - \mu_{\mathrm{closed}}$ in their magnetic momenta this can be achieved trough a homogenous magnetic offset field.

The effective scattering length is then given by the background scattering length a_{bg}, the position of the pole B_0 and the width of the resonance ΔB [16]:

$$a = a_{\mathrm{bg}} \left(1 - \frac{\Delta B}{B - B_0}\right) \tag{2.23}$$

The width of the resonance

$$\Delta B \propto \frac{g^2}{\Delta\mu\, a_{\mathrm{bg}}} \tag{2.24}$$

depends quadratically on the strength of the coupling g between the two channels, which is understandable, as the resonance is a second-order process.

^{6}Li Feshbach resonances

A $\left|F = \frac{1}{2}, m_{\mathrm{F}} = \pm\frac{1}{2}\right\rangle$ spin mixture of ^{6}Li exhibits two s-wave Feshbach resonances, which are caused by the triplet channel coupling to the weakest molecular state of the singlet potential at $\nu = 38$ through the hyperfine interaction.

The molecular state is split into two hyperfine states with nuclear spins $I = 0$ and $I = 2$, so there are two resonances, each one coupling to one of these states. The $I = 0$ state is weakly coupled to the triplet state, which leads to a narrow resonance at 534G. The $I = 2$ state on the other hand exhibits a very strong coupling to the triplet state resulting in a very wide resonance centered at 834G, with $\Delta B = 300$G and $a_{\mathrm{bg}} = -1405 a_0$ [17].

One should note that due to the large width the condition of a_{bg} being constant over the resonance implicit in eqn. 2.23 is not that well fulfilled for this resonance, but the approximation is good enough for our purposes.

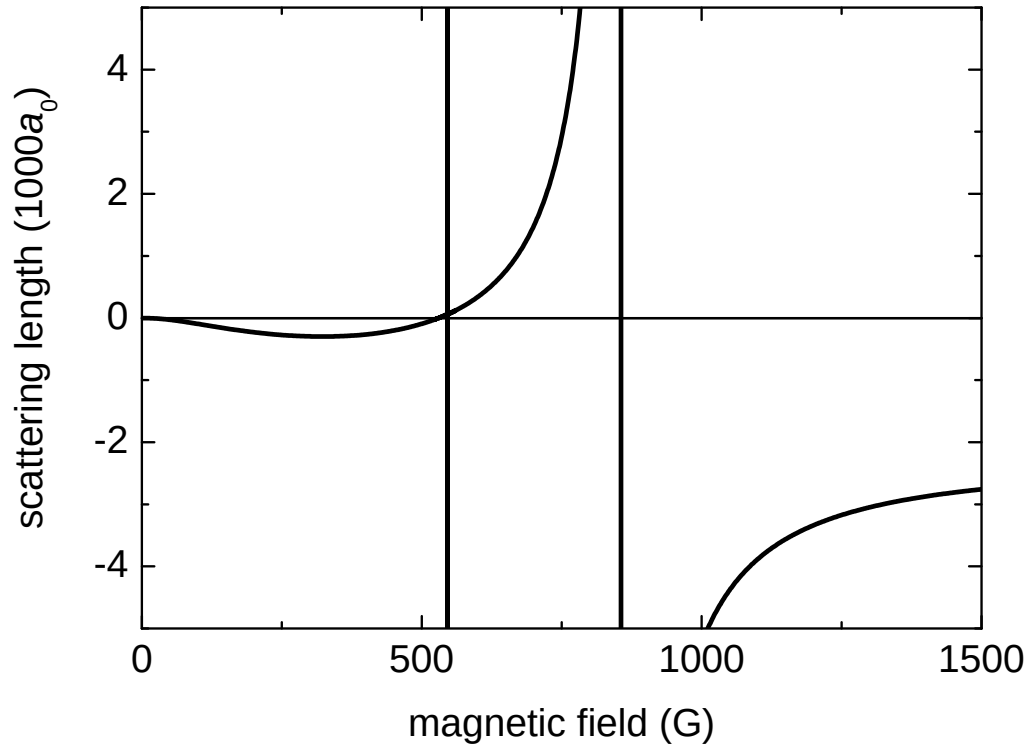

Figure 2.3: The magnetic field dependence of the s-wave scattering length for a $\left|F = \frac{1}{2}, m_{\mathrm{F}} = \pm\frac{1}{2}\right\rangle$ spin mixture of ^{6}Li. The scattering length is almost exactly zero if no magnetic field is applied. It becomes negative with growing magnetic field due to the increasing weight of a_{tr} when the electronic spins are polarized, until the effects of the wide feshbach resonance at 834 G become dominant and cause $a \to +\infty$ for $B \to 834$ G. Across the resonance a returns from $-\infty$ and for values over 1500 G is given by the triplet scattering length $a_{\mathrm{tr}} \approx -2240\, a_0$. Figure taken from [15].

Production and stability of $^6Li_2$ dimers

A large positive scattering length is always connected with a bound state of energy

$$E_\mathrm{b} = \frac{\hbar}{ma^2}, \tag{2.25}$$

these pairs of $^6\mathrm{Li}$ atoms can be viewed as very weakly bound molecules, albeit very exotic ones as the distance between the particles is much larger than the effective range R_e of their van-der-Waals interaction. The scattering length of these dimers is connected to the scattering length between unbound atoms by $a_\mathrm{da} = 1.2a$ for dimer-atom and $a_\mathrm{dd} = 0.6a$ for dimer-dimer collisons.

When the scattering length is reduced the pairs smoothly turn into ordinary $^6\mathrm{Li}_2$ molecules in the highest vibrational state. The electronic wavefunction changes from a purely triplet to a singlet form, so one of the nuclear spins has to flip to conserve total angular momentum.

If this process happens slowly it is completely reversible, fermionic clouds can be changed into bosonic molecules and back by simply ramping the magnetic field across the resonance. At sufficently low temperature of the sample this leads to the phenomenon of the BEC-BCS crossover of a degenerate quantum gas.

In principle magnetic field ramps can be used to create molecules on all feshbach resonances, but the stability of the produced dimers varies greatly. In purely bosonic systems the observed lifetimes are very short, while dimers consisting of fermionic atoms live much longer. This can be attributed to the fact that for a collisional decay of a molecule into a lower vibrational state three fermionic particles have to approach to a distance $r \approx R_\mathrm{e}$. Two of these are necessarily identical, which leads to Pauli blocking. A detailed study of inelastic atom-dimer and dimer-dimer collisions reveals that these processes scale with $a^{-3.3}$ and $a^{-2.5}$ respectivly and are therefore strongly suppressed against elastic collisions for large scattering lengths [18].

In $^6\mathrm{Li}$ the lifetime of the molecules can exceed ten seconds, which opens another way to effectively produce molecules that is so far unique to this species. Apart from adiabatically ramping across a feshbach resonance, molecules can also be formed through the more "conventional" process of reactive collisions. Of course, if the relaxation of those molecules happens fast compared to the formation, this will only lead to losses from the sample. But $^6\mathrm{Li}_2$ molecules live long enough that a chemical equilibrium between atoms and molecules can form. By setting up the partition function and minimizing the free energy $F = -k_\mathrm{b}T \ln Z$ of the system one finds

$$\Phi_\mathrm{m} = \Phi_\mathrm{N}\Phi_{\mathrm{N}'} \exp \frac{E_\mathrm{b}}{k_\mathrm{b}T}, \tag{2.26}$$

for the molecular phase space density $\Phi_\mathrm{m} = N_\mathrm{mol}/Z_\mathrm{mol}$, where Φ_N and $\Phi_{\mathrm{N}'}$ are

the phase space densities of the atoms in the two spin states. Assuming equal trap parameters and therefore equal partition functions for atoms and molecules this leads to

$$\frac{N_{\mathrm{mol}}}{N_{\mathrm{at}}} = \Phi_{\mathrm{at}} \exp \frac{E_{\mathrm{b}}}{k_{\mathrm{b}} T}, \tag{2.27}$$

where the assumption of a balanced spin mixture allows to use $\Phi_{\mathrm{N}} = \Phi_{\mathrm{N}'} = \Phi_{\mathrm{at}}$.

So if one starts with a "'hot"' sample out of the MOT and evaporativly cools it, molecules will begin to form as temperature decreases, and for $k_{\mathrm{b}} T \ll |E_{\mathrm{b}}|$ dominate the sample [19].

2.3 Evaporative cooling

As mentioned above, the phase space density in a lithium MOT is limited to values below 10^{-4}, so to reach degeneracy an increase by a factor of 10^5 is required. The method of choice to close this gap is evaporative cooling.

In this section we will briefly describe how it works and give an approximation for the efficency of the process in an optical dipole trap. Afterwards we will shortly discuss the effects of molecule formation at low temperatures.

2.3.1 Principles of evaporative cooling

The basic idea of cooling by evaporation is to selectively remove particles from the sample which have an energy much higher than the thermal energy. After rethermalization the temperature of the remaining atoms will be reduced, at the expense of a decrease in particle number. The efficeny of the evaporation – which is the ratio of phase space density gain to particle loss – and the starting conditions determine how many degenerate atoms can be produced.

Every removed particle has to have an energy at least equal to the trap depth U, so only a fraction $\exp(-U/k_{\mathrm{b}} T) = \exp(-\eta)$ of the particles can leave the trap. $\eta = U/k_{\mathrm{b}} T$ is called the truncation parameter. So if one loads a thermal gas into a trap of finite depth and waits, temperature will decrease over time. This process is called plain evaporation. In an ideal trap without heating or inelastic losses, the sample would cool down to zero temperature, with $\eta \to \infty$ for $T \to 0$. But as the speed of the evaporative cooling drops exponentially with η, in a real trap an equilibrium forms when the cooling rate is compensated by heating through intensity noise or photon scattering. In an optical trap plain evaporation typically stagnates at values of $\eta \leq 10$, depending mostly on the heating rate.

To further cool the sample after it has reached equilibrium the trap has to be lowered, which is called forced evaporation.

Following a model described by the group of J. Thomas [20], we assume a harmonic trapping potential $U(t)$ which is lowered as a function of time. The lost particles will be scattered into states just in the continuum, taking the energy $E_\mathrm{l} = U + \alpha k_\mathrm{b} T$ with them, where $\alpha k_\mathrm{b} T$ is the average kinetic energy of the particles leaving the trap. In a harmonic trap $\alpha = (\eta - 5) / (\eta - 4)$ for $U \gg k_\mathrm{b} T$. The change in total energy, taking into account the change in the average potential energy $(\dot{U}/U)E/2$ of the particles through the changing trap depth is given by

$$\dot{E} = \dot{N} (U + \alpha \, k_\mathrm{b} \, T) + \frac{\dot{U}}{U} \frac{E}{2}. \tag{2.28}$$

If one assumes η to be constant over the whole evaporation process, solving this equation leads to the scaling law

$$\frac{N}{N_0} = \left(\frac{U}{U_0} \right)^{3/(2(\eta'-3))}, \tag{2.29}$$

where N_0 and U_0 are the initial values at $t = 0$ and $\eta' = \eta + \alpha$. Using the classical phase space density in the harmonic oszillator $\rho = N(\hbar\bar{\omega})^3/(k_\mathrm{b}T)^3$ one finds that the phase space density scales as

$$\frac{\rho}{\rho_0} = \left(\frac{U_0}{U} \right)^{\frac{3(\eta'-4)}{2(\eta'-3)}} = \left(\frac{N_0}{N} \right)^{\eta'-4}. \tag{2.30}$$

If the truncation parameter is known one can use this equation to get a rough guess of the influence the initial values of atom number, mean trap frequency and temperature have on the size of the BEC. Assuming a typical value of $\eta' = 10$ one gets the relation

$$N \propto N_0^{1+\frac{1}{6}} \sqrt{\frac{\bar{\omega}}{T}} = \kappa, \tag{2.31}$$

which gives a parameter for optimizing the the initial conditions for forced evaporation.

One should note that the assumption of $\eta = const$ implies that the trap is lowered slowly compared to thermalization speed of the gas, which is given by the rate of elastic collisions $\gamma = n\sigma v$ between particles. As a higher value of η increases efficency at the cost of the evaporation being slowed by a factor $\propto \exp(\eta)/\gamma$, the optimum value of η during forced evaporation depends on the heating, losses through collisions with photons or the background gas and the rate of eleastic collisions.

In the case of s-wave scattering independent of particle momentum γ scales with n. As the trap becomes more shallow, the density inside the trap decreases, and

the rate of collisions scales with

$$\frac{\gamma}{\gamma_0} = \left(\frac{U}{U_0}\right)^{\frac{\eta'}{2(\eta'-3)}}, \tag{2.32}$$

so rethermalization takes longer at lower trap depths. But fortunately for ^{6}Li the scattering length can be tuned to large enough values that the gas is in the unitary limit, where $\sigma \propto \frac{1}{k^2}$. Thus the cooling partly compensates the decrase in density and $\gamma \propto n\frac{1}{k}$, which allows to complete evaporative cooling to degeneracy in less than three seconds [21].

2.3.2 Evaporation of atom-molecule mixtures

As mentioned in section 2.2.2 molecules are produced in 3-body-collisions during evaporative cooling on the repulsive side of the resonance. If $E_\mathrm{b} < U$ the newly formed molecule and the atom carrying the excess binding energy remain trapped and are quickly cooled to the temperature of the sample. The ratio of atoms to molecules as the cloud cools down is given by eqn. 2.27.

As the polarizability of the molecules can be described simply as the sum of the polarizabilities of the individual atoms, the molecules see a trap depth twice as large as the atoms, leading to $\eta_\mathrm{m} = 2\,\eta_\mathrm{at}$. Therefore the evaporation of molecules from the trap is exponentially suppressed against the evaporation of atoms.

When atoms are lost from the trap through forced evaporation some molecules have to be dissociated into atoms to maintain the chemical equlibrium. These thermalize with the molecules and after some time evaporate from the trap, taking the energy $2E_\mathrm{at} = 2(\eta_\mathrm{at} + \alpha)k_\mathrm{b}T$ with them. As usually $\alpha \ll \eta$ the cooling effect is roughly equivalent to the evaporation of one molecule with $\eta_\mathrm{mol} = 2\eta_\mathrm{at}$. The speed of the evaporation on the other hand depends on η_{at}, which determines the probability of the atoms being scattered into a state with $E > U$. This gives the possibility to evaporate molecules with very high efficency [19].

One should note that if reestablishing the chemical equilibrium takes longer than the thermalization of the sample it replaces the rate of elastic collisons as bottleneck of the evaporation process. But as the rate coefficents for molecule formation and dissociation scale with a^6 [22], the chemical equilibrium is restored quickly compared to the thermalization for sufficently large scattering length.

2.4 Key properties of BECs

Quantum phenomena begin to dominate the behavior of a dilute gas when the De Broglie wavelength of the particles is of the order of the interparticle separation.

This is equivalent to the phase space density, which describes the ratio of the particle number N to the number of available states Z

$$\Phi = \frac{N}{Z} = n^3 \lambda_{\mathrm{db}}^3, \tag{2.33}$$

where

$$\lambda_{\mathrm{db}} = \sqrt{\frac{h}{2\pi m k_{\mathrm{b}} T}} \tag{2.34}$$

is the thermal De Broglie wavelength, reaching unity. This regime is called quantum degenerate.

To properly describe a degenerate Bose gas the classical Boltzman distribution function has to be replaced by the Bose distribution

$$f(E_\nu) = \frac{1}{e^{(E_\nu - \mu)/k_{\mathrm{b}} T} - 1}, \tag{2.35}$$

where $f(E_\nu)$ gives the mean occupation number of the single particle state ν with energy E_ν. We will discuss some of the consequences of this diffference in the next sections, generally following the arguments given in [23].

2.4.1 Critical temperature and condensate fraction

To calculate the number of particles in the gound state one sums eqn. 2.35 over all excited states and substracts the result from the total particle number:

$$N_0 = N - N_{\mathrm{ex}} = N - \sum_{\nu \neq 0} \frac{1}{e^{(E_\nu - \mu)/k_{\mathrm{b}} T} - 1} = N - \int_0^\infty dE\, g(E) f(E), \tag{2.36}$$

where the sum has been replaced by an integral over the density of states $g(E)$ in the last step.

The critical temperature T_{c} is the temperature where the ground-state population starts to become macroscopic, which is equivalent to all particles being in excited states while all additional particles added to the system would have to be in the ground state. Assuming non-interacting particles and neglecting the energy of the ground state this gives the conditions $N = N_{\mathrm{ex}}$ and $\mu = 0$, leading to

$$N = N_{\mathrm{ex}}(T_{\mathrm{c}}, \mu = 0) = \int_0^\infty dE\, g(E) \frac{1}{e^{E/k_{\mathrm{b}} T_{\mathrm{c}}} - 1} \tag{2.37}$$

Solving this integral for the density of states of an harmonic oszillator potential one obtains

$$k_{\mathrm{b}} T_{\mathrm{c}} = \frac{\hbar \overline{\omega} N^{1/3}}{\xi(3)^{1/3}} \approx 0.94 \hbar \overline{\omega} N^{1/3} \tag{2.38}$$

for the critical temperature, where $\overline{\omega} = (\omega_1\omega_2\omega_3)^{1/3}$ is the mean trap frequency and $\xi(\alpha) = \sum_{n=1}^{\infty} n^{-\alpha}$ is the Riemann Zeta function.

Evaluating eqn. 2.36 for a given temperature T and using the critical temperature T_c gives the condensate fraction

$$N_0 = N\left(1 - \left(\frac{T}{T_\mathrm{c}}\right)^3\right). \tag{2.39}$$

Although equations 2.38 and 2.39 were derived for the case of an ideal gas, they can still be applied to weakly interacting condensates with $na^3 \ll 1$.

2.4.2 Density distribution of a BEC in the ground state

The density distribution of a BEC in a trap is given by the absolute square of its many-body wavefunction

$$\Psi(\mathbf{r}_1, r_2, \ldots, r_N) = \prod_{i=1}^{N} \Phi(\mathbf{r_i}). \tag{2.40}$$

For an ideal gas at zero temperature all particles are condensed in the lowest single-particle state Φ_0, and the density distribution $n(\mathbf{r}) = N\left|\Phi_0(\mathbf{r})\right|^2$ can be easily calculated by solving the Schrödinger equation

$$i\hbar\frac{\partial}{\partial t}\,\Phi_0(\mathbf{r},t) = \left(\frac{\hat{p}^2}{2m} + V(\mathbf{r})\right)\,\Phi_0(\mathbf{r},t) \tag{2.41}$$

for a single particle in the given trapping potential $V(\mathbf{r})$.

But as soon as interactions between particles are considered, things get a lot more complicated. If the cloud is dilute, which is equivalent to the average interparticle distance being larger than the scattering length, the interactions between the particles can be approximated by an effective interaction $g\,\delta(\mathbf{r} - \mathbf{r_0})$, where $g = \frac{4\pi\hbar^2 a}{m}$ is the strength of the coupling. Setting up the total energy of the system and minimizing it through a variational approach leads to the Gross-Pitaevskii equation

$$i\hbar\,\frac{\partial}{\partial t}\,\Psi(\mathbf{r},t) = \left(\frac{\hat{p}^2}{2m} + V(\mathbf{r}) + g\left|\Psi(\mathbf{r},t)\right|^2\right)\,\Psi(\mathbf{r},t), \tag{2.42}$$

which has the form of a nonlinear Schrödinger equation in which the interactions are approximated by a mean field depending only on the density $\left|\Psi(\mathbf{r},t)\right|^2$ and the strength of the coupling g.

To find the ground state of the system one can use a time independent formulation by setting $\Psi(\mathbf{r},t) = \Psi(\mathbf{r})e^{-i\mu t/\hbar}$, which leads to the time-independent Gross-Piteavskii equation

$$\left(\frac{\hat{p}^2}{2m} + V(\mathbf{r}) + g\left|\Psi(\mathbf{r},t)\right|^2\right)\Psi(\mathbf{r}) = \mu\Psi(\mathbf{r}). \tag{2.43}$$

This is a nonlinear differential equation and therefore hard to solve analytically. Fortunately in most systems the interaction energy is much larger than the zero-point-motion of the particles and the kinetic energy term can be neglected.

This is called the Thomas-Fermi approximation, which causes equation 2.43 to simplify to $\mu = V(\mathbf{r}) + g\,\Psi(\mathbf{r})$ with the solution

$$n(\mathbf{r}) = \left|\Psi(\mathbf{r})\right|^2 = \frac{(\mu - V(\mathbf{r}))}{g} \tag{2.44}$$

for $\mu - V(\mathbf{r}) > 0$ and $\Psi = 0$ otherwise. From this follows $\mu = V(\mathbf{r})$ as a condition for the size of the cloud. Assuming an harmonic oszillator potential , one obtains the Thomas-fermi radii

$$R_{\mathrm{i}} = \sqrt{\frac{2\mu}{m\omega_{\mathrm{i}}}},\ i = 1,2,3 \tag{2.45}$$

at which the condensate wavefunction drops to zero. From equation 2.44 and the normalization condition of the wavefunction $N = \int d\mathbf{r}\ \left|\Psi(\mathbf{r})\right|^2$ follows the chemical potential

$$\mu = \frac{\hbar\bar{\omega}}{2}\left(\frac{15Na}{\bar{a}}\right)^{2/5} \tag{2.46}$$

with the mean harmonic oszillator length $\bar{a} = \sqrt{\frac{\hbar}{m\bar{\omega}}}$.

Chapter 3

Experimental Setup

Creating a BEC requires the application of many different experimental techniques, as one has to provide a ultra-high vacuum environment as well as stable laser light to trap and image the atoms. In the case of ^{6}Li one additionally has to be able to create homogenous magnetic fields of $800\,\mathrm{G}$ to form bosonic molecules which can be condensed. This chapter aims to not only describe the key elements of our setup, but also to explain the reasoning behind our design choices whereever possible.

As the details of the vacuum setup, the lithium oven and the magnetic field coils for MOT and Zeeman slower have already been described in the diploma thesis of Friedhelm Serwane [10], the focus will be on the laser systems for trapping and imaging, the coils used for producing large homogenous offset fields and the experiment control.

3.1 Vacuum system

Our vacuum system consists of two main sections: The oven chamber, where lithium is evaporated in an oven at a temperature of 300°C to 400°C, and the experimental chamber where the atoms are captured in the MOT.

These two elements are connected by a 30 cm-long stainless steel tube, which serves both as a drift tube for the Zeeman slower and as a differential pumping section to maintain the pressure difference beetween the experimental chamber, which is at a pressure of $p \approx 10^{-12}$ mbar and the oven chamber, whose pressure is limited to 10^{-10} mbar by the outgassing of the heated Lithium. The vacuum is maintained by a combination of titanium sublimation and ion getter pumps, which have the distinct advantage of working without noise or vibrations.

The key part of the apparatus is a spherical octagon (Kimball Physics MCF600-SO200800-A), on which 6 CF40 viewports and two reentrant viewports provide

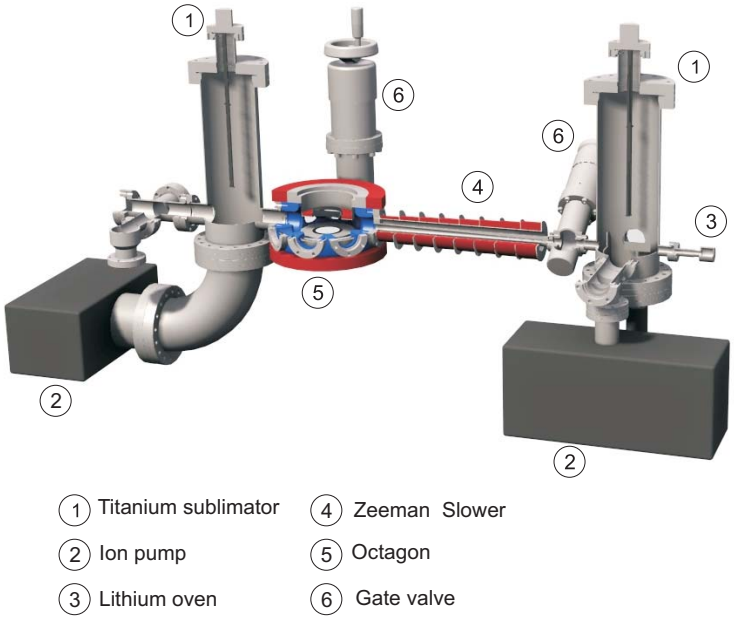

Figure 3.1: Overview of the vacuum setup with the oven chamber on the right and the octagon on the left. The magnetic field coils for Zeeman slower, MOT and Feshbach fields are shown in red. The gate valve (6) gives us the option to insert upgrades into the octagon or add an additional science chamber without breaking the vacuum.

adequate optical access.

Around the chamber a large solid aluminum breadboard provides generous space for our MOT and dipole trap optics. The surface of the breadboard is set 10 cm below the center of the octagon, so that all beams in the horizontal axis can be prepared at a convenient height and sent directly through the CF40 viewports.

3.2 671nm laser System

All 671nm laser light we need for the MOT and absorption imaging is prepared on a separate optical table and brought to the experiment through single-mode polarization maintaining optical fibers. We use two grating stabilized extended cavity diode lasers (DL 100, Toptica, 25mW) and one tapered amplifier system (TA 100, Toptica, 500mW), consisting of one more diode laser and a tapered amplifier chip, to produce the laser light needed for the MOT and absorption imaging. An outline

of the setup can be found in fig. 3.3.

3.2.1 Frequency reference and offset locks

To effectively use near-resonant light for manipulating atoms we must stabilize and control its frequency to a few hundred kHz. As the frequency changes of our lasers due to thermal drifts and vibrations are several orders of magnitude larger, we have to actively stabilize them.

The starting point for this is one diode laser which is stabilized to the $F = \frac{3}{2} \rightarrow F = \frac{5}{2}$ line of the $s_{\frac{1}{2}} \rightarrow p_{\frac{3}{2}}$ transition of ^{6}Li, which is the main cooling transition of our MOT. The stabilization is done with a feedback loop, which varies the position of the grating in the diode laser with a piezoelectric crystal. This changes the length and thereby the resonance frequency of the extended cavity. The error signal for the feedback loop is created by frequency modulation spectroscopy of lithium vapor in a stainless steel tube heated to ~300°C. The stabilized laser can be used as a frequency reference, to which we lock our MOT and imaging lasers via offset locks.

We overlap the laser we need to stabilize with our reference laser on an amplified fast photodiode (PDA10A-EC, Thorlabs) using about $100\,\mu$W of power from each laser. Due to the interference between the lasers the photodiode detects an intensity modulation of the light at the beat frequency $\nu = |\nu_1 - \nu_2|$ of the two lasers. Using a relatively simple electronic setup (see fig. 3.2) consisting of self-contained RF-components from MiniCirciuts we create an error signal from this beat note.

We start by mixing the photodiode signal with a sine wave at ν_{VCO} from a voltage controlled oscillator (VCO). The sum frequency is filtered out with a low pass filter, and the difference frequency $\Delta\nu = \nu - \nu_{\mathrm{VCO}}$ is split up and recombined on a second mixer, after one part has been delayed by 2 meters of coaxial cable. By filtering out the sum frequency after the second mixer we get a DC signal proportional to the cosine of the phase difference $\Phi = \tau \cdot \Delta\nu$ induced by the delay line. The zero crossings of this signal can be used as locking points for the PID-controller [24].

As the phase difference depends on the frequency of the VCO, the locking point, and thereby the frequency of the laser, can be easily tuned over the dynamic range of the VCO without breaking the lock if one takes care not to exceed the limitations of the servo loop. This ability is crucial for an optimal transfer of the atoms from the MOT into the dipole trap.

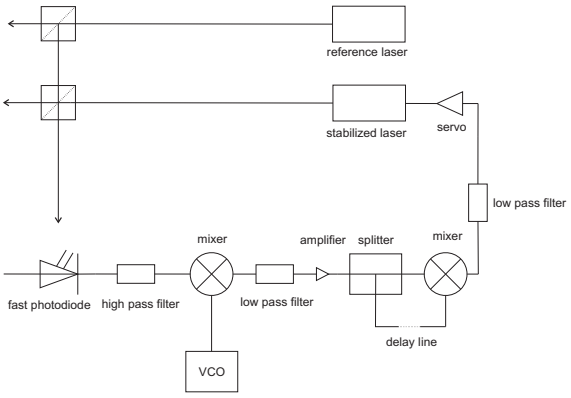

Figure 3.2: Schematic of the beat offset lock used to stabilize the MOT and imaging lasers to our frequency reference.

3.2.2 Magneto-optical trap

Preparing MOT and Zeeman slower light

The laser power we need for our MOT and the Zeeman slower beam is provided by a TA100 tapered amplifier system (Toptica). It contains one diode laser identical to our spectroscopy laser, which we can lock to our desired wavelength, and one tapered amplifier chip which amplifies the beam to about 500 mW.

In lithium the dipole transitions from the ${}^2S_{\frac{1}{2}}$ ground state to the ${}^2P_{\frac{3}{2}}$ excited state are not really closed at low magnetic field due to the fact that the hyperfine splitting of the exited state is smaller than the natural linewidth, so an about equal amount of laser power is needed for both hyperfine states of the ground state.

Therefore we lock the TA relative to the crossover between the $F = \frac{3}{2}$ ("cooler") and $F = \frac{1}{2}$ ("repumper") transitions, which have a splitting of 228 MHz. The power is split on a polarizing beamsplitter (PBS) and two acousto-optic modulators (MTS114-B10A3-671, AA Optoelectronics) shift the light by $\pm 114\,\mathrm{MHz}$ respectivly. We achieve maximum loading rates at a ratio of cooling to repumping light of approximately 2:1.

After passing through telescopes to match the beam size to the fiber couplers both beams are overlapped again in a 50/50 non polarizing beamsplitter. One of the resulting beams is split equally and coupled into two optical fibers; these provide the light for the horizontal MOT beams. The other beam is divided into a larger and a smaller part. The smaller part is directly coupled into a fiber and serves as the vertical MOT beam, while the rest is red-shifted by 70 MHz using an AOM (Crystal Technologies, model 3080-125) and used for the Zeeman slower.

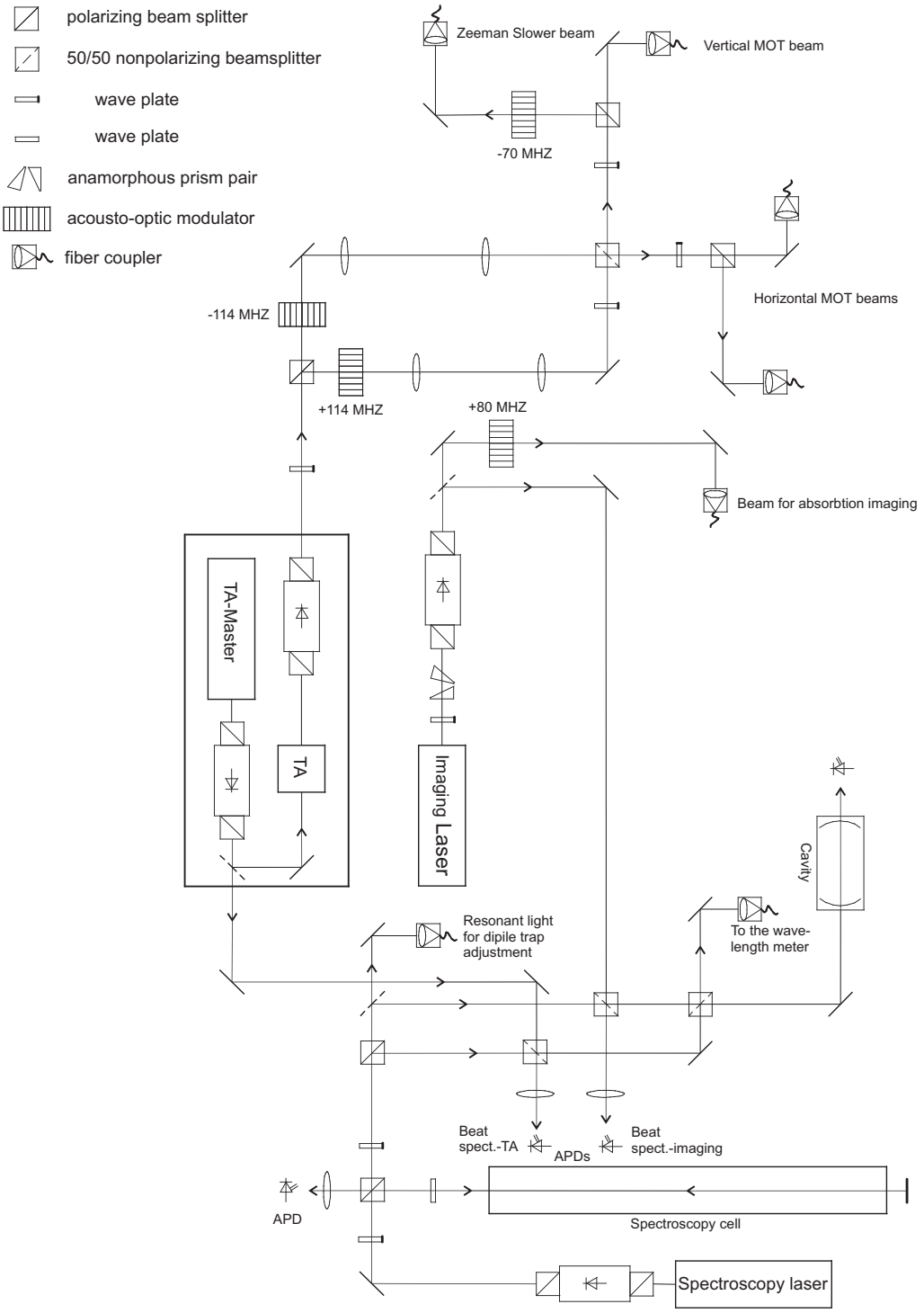

Figure 3.3: Overview of the 671 nm laser system

Setup of MOT and Zeeman slower

The coils which produce the quadrupole field necessary for the MOT are mounted directly on the octagon, around the CF100 flanges of the reentrant viewports. This has the advantage that the coils - and therefore the zero of the magnetic field as well - are intrinsically aligned to the center of the octagon. This greatly simplifies the coarse adjustment of the MOT and dipole trapping beams. The coils are operated at a current of 32 A and deliver a magnetic field gradient of 20 G/cm in the weak and 40 G/cm in the strong axis.

The fiber connector and all the optical elements to create a circularly polarized one inch diameter MOT beam are contained in a single lens tube assembly (SM, Thorlabs).

The light emerges from the fiber linearly polarized with a NA ~ 0.1. To get a circular polarization the expanding beam passes trough a true zero order $\frac{\lambda}{4}$-plate; to adjust the polarization the fiber connector can be freely rotated in the lens tube and is fixed at the desired angle with a nylon screw. The beam is collimated by a $f = 100$ mm lens, with a diameter $d \approx 23$ mm. An integrated Iris enables us to reduce the size to $d \approx 3$ mm for precise adjustment of the beams.

The whole assembly is placed in a SM slip ring and mounted on a kinematic prism mount (KM100P, Thorlabs) for angular adjustment. The beams are retroreflected using a one inch $\frac{\lambda}{4}$-plate and mirror combination in a lens tube on a SM mirror mount (KM100T, Thorlabs). Thus the MOT optics around the chamber consist of only six compact elements.

A slight disadvantage of this setup is that the beam is almost as big as the collimating lens, which leads to diffraction effects and consequently a bad beam profile in the far field, which limits the distance to the octagon at which we can place our MOT optics.

Our Zeeman slower has a decreasing field configuration that uses the radial MOT field as the last part of the magnetic field, which allows for a quite compact design. The disadvantage is that both the magnetic field and - due to the relatively small additional detuning - the slowing laser have a rather large influence on the position of the MOT.

The magnetic field is produced by eight coils centered around the drift tube and the radial component of the MOT field. The drift tube opens up from an aperture of 5 mm at the oven side to 16 mm at the flange to the octagon, which increases the solid angle under which atoms evaporated from the oven can reach the MOT. Additionally, the adverse effect of transversal heating through the slowing process should be somewhat alleviated by this geometry. The calculations to this can be found in [10].

The laser beam is prepared in another lens tube assembly. It expands to a diameter of $d \approx 35$ mm from the fiber and passes through a lens array with an effective

focal length of $f \approx 133\,\mathrm{mm}$, which leads to a slightly convergent beam. The convergence angle and the distance of the lenses to the Zeeman slower drift tube are chosen such that the size and convergence of the beam mirror the shape of the drift tube. By this we try to optimize the laser intensity for the changing size of the atomic beam.

Performance of the MOT

We have found that operating the MOT at a detuning of $\delta_{\mathrm{MOT}} \approx -7\,\Gamma$ is a good compromise between the loading rate, which could be increased by 20% at a detuning of $\delta_{\mathrm{MOT}} \approx -10\,\Gamma$, and a precise control of the frequency (for details on the limitations of our beat lock see [24]).

The loading rate of the MOT depends strongly on the temperature of the Lithium oven, it rises from $L \approx 10^7\,\frac{\mathrm{atoms}}{\mathrm{s}}$ to $L \approx 10^9\,\frac{\mathrm{atoms}}{\mathrm{s}}$ if the oven temperature is increased from $T = 300\,°\mathrm{C}$ to $T = 400\,°\mathrm{C}$.

For most experiments an atom number of $N \approx 10^8$ atoms is sufficient, we can load those in $t_l = 1\mathrm{s}$ at an oven temperature of $340°\mathrm{C}$. This enables us to do our experiments with quite large repetition rates.

The limitations of our setup become visible when we try to push towards large particle numbers in the MOT. At an oven temperature of $T = 400\,°\mathrm{C}$ the MOT saturates after a loading time of $t_l \approx 3\mathrm{s}$ at $N \approx 10^9$ atoms. A six beam MOT using larger beams and a larger detuning would probably raise the maximum particle number, but the number achievable with our current setup should be sufficient for the kind of experiments we are planning to conduct in our apparatus.

A very pleasant surprise has been the resilience of our MOT: The lasers work very reliable, only rarely needing minimal adjustment. The fiber couplings are quite stable, readjustments are neccessary about once a week or less. As the adjustment of the outcouplers and retroreflectors has proven to be uncritcal as well, we are free to focus on other, more critical parts of the experiment.

A more detailed examination of the MOT parameters can be found in [10].

3.2.3 Imaging systems

At the moment we have two diagnostic tools available to get information about our trapped atoms. The first is recapturing the atoms in the MOT and measuring the fluorescence. This yields information about the number of particles. The second one is absorption imaging, which additionally gives the column density of the atomic cloud in the viewing axis. It is the main tool used for examining ultracold atoms.

Fluorescence images of the MOT

To determine the properties of our MOT, and to measure the number of particles in our dipole trap, we take fluorescence images of our MOT. The light is collected by a 25mm diameter lens with $f = 150\,\mathrm{mm}$ placed in front of a CF40 viewport so that the MOT lies in the focal plane. A second lens with $f = 150\,\mathrm{mm}$ focuses the light on a CCD camera (GUPPY F-038B NIR, AVT), which proved to be a very good choice due to its high sensitivity and easy handling.

To derive the particle numbers from the images taken by the camera we have to establish a calibration. The first step is to convert the arbitrary units of the camera ADC into photon numbers, the conversion factor is determined by shining a laser beam into the imaging system, whose power has been measuerd with a calibrated power meter (PD-300-<TP-SH, BFI Optilas).

The next step is to take an image of a small atomic cloud right on resonance, and use the formula

$$N = \frac{N_{\mathrm{phot}}}{2\pi\Gamma}\frac{4\pi}{\Omega}\frac{1}{t_{\mathrm{exp}}}, \tag{3.1}$$

where Ω is the solid angle captured by the camera optics, to calculate the particle number.

This formula requires that the optical transition is completely saturated, so that the atoms radiate photons whith the full resonant scattering rate $2\pi\,\Gamma \approx 36\,\mathrm{MHZ}$ and saturation effects like reabsortion can be neglected, which can only be simultaneously fulfilled for small clouds. By measuring the particle number of a small sample and using the result to determine the fluorescence at a detuning of $20\mathrm{Mhz}$, where saturation effects become much less critical, one can obtain a conversion from camera counts at a certain detuning to particle numbers, which is valid for large clouds as well. For our setup we get a conversion factor of

$$\kappa = 76\frac{\mathrm{atoms}}{\mathrm{count}\cdot\mathrm{ms}} \tag{3.2}$$

at a detuning of 20 MHz [10]. The error based on the uncertainty in the solid angle is about 20%, but the effects of saturation and reabsorption are hard to quantify. As those effects can only reduce the amount of flourescent light these measurements give a lower bound for the number of atoms in the MOT.

Although the error of the absolute particle number is quite large and not well known, most errors drop out when only the ratio between two particle numbers has to be measured. As this is the quantity of interest for almost all of our measurements, recapturing the atoms into the MOT and measuring their fluorescence is an easy and robust way to determine trap lifetimes and transfer efficiencies as well as trap frequencies through the measurement of resonant losses.

Absorption imaging

For taking absorption pictures we use the same optics and camera as for the fluorescence imaging. The light for the absorption beam comes from another diode laser locked to our frequency reference laser. The photodiode used for the beat lock (Hamamatsu G4176-03) has a bandwidth of 6 GHz, which allows us to lock the imaging laser at the large detunings neccessary for imaging in high magnetic fields. The camera is placed under an angle of 45°to the axis of the dipole trap, for details see figure 3.4.

When taking absorption images it is customary to take three pictures in quick succession: The first is the actual absorption image of the atomic cloud, the second one is the reference picture which is taken under identical conditions as the first picture, with the only exception that there are no atoms present. The third one is a background picture without the absorption beam, which is subtracted from the other pictures. The big advantage of this technique is that by dividing the counts of the absorption image with the ones from the reference picture one directly gets the value of the optical density

$$OD = -\ln \frac{I_{abs} - I_{bg}}{I_{ref} - I_{bg}} \tag{3.3}$$

for each pixel, while effects like intensity and inhomogenity of the imaging beam drop out, as do interference fringes, given that they are the same on both images. Therefore it is of vital importance to avoid vibrations of the imaging setup, which would cause the fringe patterns to move.

If the absorption cross section is known, the column density

$$n(x, y) = \int \mathrm{d}z\, \rho(x, y, z) = \frac{OD}{\sigma} \tag{3.4}$$

of the atomic cloud can be calculated from the optical density. The transitions we are using require σ-polarized light, but as the imaging beam is running perpendicular to the magnetic field axis, we use horizontially polarized light and get a cross section of

$$\sigma = \frac{3\lambda^2}{4\pi}, \tag{3.5}$$

in high magnetic fields, which is half the value for properly polarized light along the quantization axis.

The main limitation for near-resonant absorption imaging is the heating of the sample by the scattered photons. Due to its low mass, the time before structure gets washed out is especially short in Lithium, therefore we illuminate the atoms only for 10μs. Additionally one has to take care that the optical density of the

cloud is close to one, as the absorption signal gets lost in the shot noise when the cloud is to thin or to dense.

With the current setup the resolution is limited by the pixel size of the CCD chip. As the only non-interlaced mode of the camera bins four pixels together, the effective pixel size is $16.8 \times 19.6\,\mu\mathrm{m}$, together with the magnification $M = 1.1$ this leads to a resolution of roughly $20\,\mu\mathrm{m}$.

Although this resolution is quite bad, it should be sufficent for preliminary experiments, and we are confident that by magnifying the image and using better optics we can further improve the resolution if it becomes neccessary, although in the end the low numerical aperture will prevent resolutions better than $10\,\mu\mathrm{m}$.

Calculating atom number and temperature from absorption images

To derive the atom number we first integrate the image along one axis and fit a gaussian distribution

$$OD(x) = a\, e^{\frac{(x-x_0)^2}{2\rho^2}} \tag{3.6}$$

to the atomic cloud, where the scale factor

$$\frac{a\rho}{\sqrt{2\pi}} = \int_{x,y} OD \tag{3.7}$$

gives the integrated optical density normalized to the area A/M^2 imaged on one pixel with size A at magnification M. Using this fit instead of summing the whole absorption signal eliminates offsets caused by different intensities of the imaging laser in the absorption and reference picture.

We get the equation

$$N = \frac{a\rho}{\sqrt{2\pi}} \frac{A}{M^2 \sigma} \tag{3.8}$$

for the total atom number N.

Atom numbers determined through flourescence and absorbtion imaging differ only by about 20%, which is well within the uncertainty of the photon scattering rates and the solid angle. Together with the fact that the difference does not change significantly over a wide range of particle numbers this gives us confidence that our measurements are realistic.

The spatial distribution of a thermal cloud in a trapping potential $U(\mathbf{r})$ has the form

$$n(\mathbf{r}) = n_0 e^{-\frac{U(\mathbf{r})}{k_B T}}, \tag{3.9}$$

assuming a harmonic potential this leads to a $\frac{1}{\sqrt{e}}$ width of $\rho_i = \sqrt{k_\mathrm{b} T / m\omega_i^2}$. If those atoms are released from the trap they expand ballistically, with momenta

according to the Boltzman distribution

$$f(\mathbf{p}) \propto e^{-\frac{p^2}{2mk_BT}}. \tag{3.10}$$

The spatial distribution $n(\mathbf{r}, t)$ after a time of flight t is the convolution of these two gaussians

$$n(\mathbf{r}, t) = \int e^{-\frac{m^2(\mathbf{r}-\mathbf{r}_0)^2}{2mt^2k_BT}} e^{-\frac{\mathbf{r}_0^2}{2\rho_0^2}} d^3\mathbf{r}_0 \tag{3.11}$$

with a $\frac{1}{\sqrt{e}}$ width of

$$\rho = \sqrt{\rho_0^2 + \frac{k_BT}{m}t^2} \tag{3.12}$$

As our resolution does not allow us to accurately determine the initial width of the cloud in the radial direction, we have to let the cloud expand far enough that ρ_0 can be neglected. If this condition is fulfilled, the error of the measurement depends mostly on the uncertainty of the magnification of the imaging system.

3.3 Optical dipole trap

When planning a trap for evaporative cooling of neutral particles one has to consider several important aspects. There are two types of traps available, magnetic and optical. As we intend to cool fermions, whose elastic cross section vanishes at ultracold temperatures for identical particles, we have to either use particles of a different species as cooling agent, or a mixture of different spin states. As we want to avoid the effort of cooling atoms of another species, and the only spin mixture of ^{6}Li stable against collisional decay is $\left|F = \frac{1}{2}, m_\mathrm{F} = \pm\frac{1}{2}\right\rangle$, which cannot be trapped magnetically, we chose an optical dipole trap.

Such a trap can be created by an intensity maximum of red-detuned light or by creating a local minimum surrounded by walls of blue-detuned light. We decided to use the first geometry, as it is much simpler. The price for this is higher laser power, as the atoms are captured in the intensity maximum and a very large detuning is neccesary to avoid excessive heating through photon scattering. Additionally the entire volume of the trap has to be filled with light, while a blue-detuned trap only needs walls.

A small volume trap can be created by one tightly focussed beam. The axial confinement is given by the radial intensity distribution of the gaussian beam, while in the longitudinal axis the trap is determined by the Rayleigh range $z_0 = \pi\omega_0^2/\lambda$ of the focus. Due to z_0 scaling with ω_0^2 these traps are usually very elongated, with aspect ratios of up to 100. This limits the maximum diameter of the focus, as the traps quickly get too shallow in the long axis, and the atoms can be pulled

out by gravity or stray magnetic field gradients. As we need a large volume of our optical dipole trap to capture as many atoms as possible from the MOT, we have to use a crossed beam setup where the trap shape is given by the overlap of the beams.

To optimize the transfer from the MOT one wants the overlap of MOT and dipole trap to be as large as possible. As the available laser power is the limiting factor, because cost and technical difficulties grow with higher power, the trap depth should be as low as possible while still capturing most of the atoms.

A further consideration is the performance of evaporative cooling. Ideally one wants a high density for high collision rates as well as a large truncation parameter for fast and efficent evaporation. The truncation parameter for a trap which barely manages to hold the atoms is of course very bad, a trap which achieves optimal transfer from the MOT suffers from a very lossy initial evaporation until the gas is cooled down enough to get a decent truncation parameter. To make matters worse, density drops when the trap becomes more shallow, so collison rates are low to begin with and get worse as soon as forced evaporation begins.

One way to deal with these contradictive requirements is a compromise between trap volume and initial depth [21], which of course decreases the number of degenerate particles that can be achieved.

We try to overcome these limitations by using time-averaged optical potentials to reshape our trap during the experiment, which should allow us to independently optimize the trap parameters for both tasks. We also hope that it will give us a way to counter the effects of thermal lensing caused by the high power beam, which turned out to be larger than expected.

The idea is to set up the optics such that at low laser power the foci of two beams with a waist of approximately $80\,\mu\mathrm{m}$ intersect in the center of the chamber, which gives a tight and well-defined trap suited for evaporative cooling. For optimized transfer from the MOT two AOMs can be used to scan the X-Y-position of the focus with a frequency much larger than the trapping frequencies, leading to a time-averaged potential of lower depth and larger volume. Additionally all structure of the beams is washed out, which leads to a very homogenous trap. As the AOMs are needed anyway for intensity stabilization and to precisely lower the trap over three orders of magnitude during forced evaporation, the additional cost and effort of this scheme are comparatively low.

3.3.1 Setup of the crossed beam trap

We use red-detuned light from a $200\,\mathrm{W}$ Ytterbium fiber laser (YLR-200-LP, IPG Photonics). The main element of the laser is an Ytterbium-doped fiber, which is at the same time the resonator and the active medium. As the fiber is single mode and polarization maintaining, the emitted beam is an almost perfect gaussian

($M^2 < 1.1$) with linear polarization. The laser emits on a several nanometer broad wavelength range centered around $1068\,\mathrm{nm}$, which reduces the coherence length to less than a centimeter and allows us to retroreflect and cross beams without creating standing waves.

The output from the fiber laser is a collimated beam with a diameter of $2.8\,\mathrm{mm}$ at low power, which shrinks to $2.4\,\mathrm{mm}$ at maximum power due to thermal effects. The beam size is first reduced to $1.3\,\mathrm{mm}$ to fit through the two AOMs used for X-Y-deflection and intensity control and then expanded again to $3.1\,\mathrm{mm}$ to achieve the desired spot size of $\omega_0 = 80\,\mu\mathrm{m}$ with our final focussing lens. While the individual AOMs cause some astigmatism, the effects of both AOMS cancel each other due to the crossed setup. The beam enters the vacuum chamber through one of the CF40 viewports on the side under an angle of 7° to the axis, the smallest angle possible with a lens of $f = 300\,\mathrm{mm}$ without clipping the MOT beam going through the same window. On the other side of the octagon the expanding beam is collimated by another lens ($f = 250\,\mathrm{mm}$), reflected across the MOT beam and focussed back into the chamber by a second lens of $f = 250\,\mathrm{mm}$ under the same angle. These two lenses clip away several millimeters of the retroreflected MOT beam, but we did not have suitable lenses with a larger focal length available. Fortunately the adverse effect on the MOT seems to be rather small, as there was no noticable degradation in the performance of our MOT after setting up the dipole trap.

The two focused beams cross in the center of the octagon under an angle of 14°. A sketch of the setup can be found in 3.4 and a graph of the calculateted trap shape in 3.5. The calculated axial and longitudinal trap frequencies at a laser power of 32W are $\omega_x = \omega_y = 2\pi \cdot 2800\,\mathrm{Hz}$ and $\omega_z = 2\pi \cdot 350\,\mathrm{Hz}$, with a maximum trap depth of $382\,\mu\mathrm{K}$.

3.3.2 Thermal lensing

The biggest challenge in setting up our dipole trap turned out to be thermal lensing, a problem which we greatly underestimated in the planning stage and whose details we still do not fully understand. One reason is that almost all optical components except the laser itself show lensing at powers above ~60 W, so it is hard to isolate the effect caused by any single element. Also there are several different mechanisms causing beam distortions and quantifying how much each contributes to the overall effect is difficult.

One of the major problems is certainly dirt on the optics, which is captured by the laser through dipole forces and accumulates on the surfaces of the optics. Another problem can be the absorption of light in the bulk material of the optics, this effect was so strong in our optical isolator (FI-1060/8 SI-HP, Linos Photonics) that we had to remove it from the setup. Absorption could also account for the

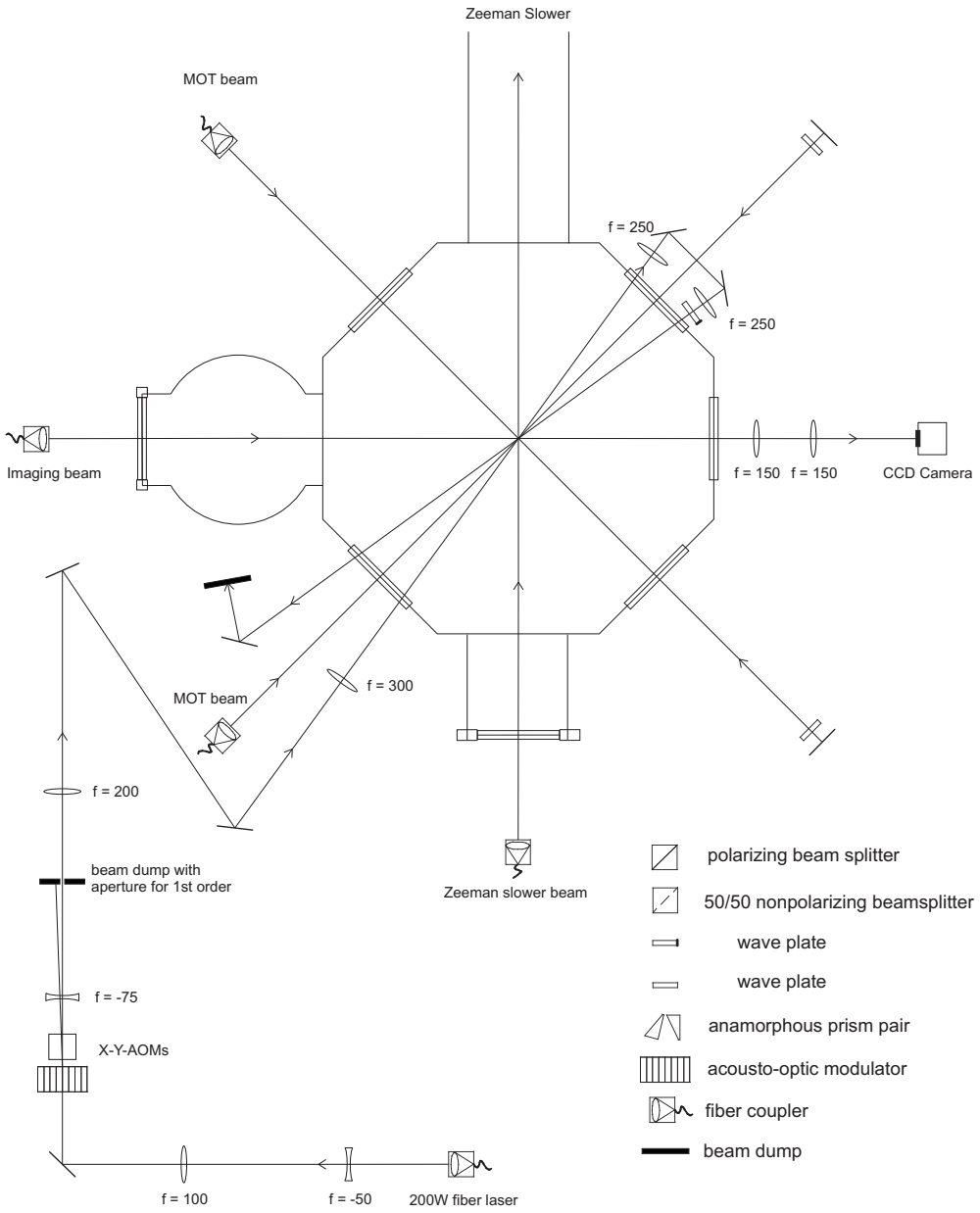

Figure 3.4: The optics for MOT, dipole trap and imaging around the octagon. The beams are prepared on a single U-shaped breadboard placed ten centimeters below the center of the octagon, so we can mount all optics on short, stable posts. Additionally we do not have to change the height of the high power beams to send them into the octagon.

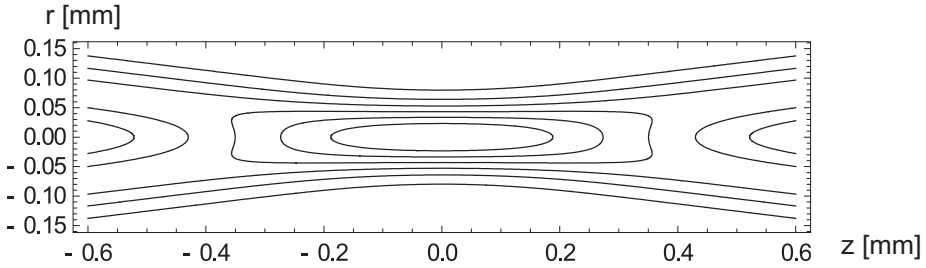

Figure 3.5: Shape of the trapping potential for two $80\,\mu$m-foci crossing under an angle of $14°$. The aspect ratio of this trap is $\omega_{\mathrm{rad}}/\omega_{\mathrm{ax}} = 8.1$.

fact that even freshly cleaned lenses show thermal effects, and fused silica optics are slighty better than the ones made of BK7. In the AOMs TeO_2 is used, which fortunately creates only minor effects, as the crystals are 20mm thick and would cause serious problems otherwise.

So far the most efficient ways to counter these problem have been to regularly clean the optics, only operate the infrared laser with the flowbox running to minimize the amount of particles in the air, and to keep the number of optical elements in the beam as small as possible.

We built up all dipole optics with the breadboard lying on a schematic drawing of the vaccum setup. This allowed us to make sure the focus of the first lens would be in the center of the octagon when we moved the whole setup in place, and gave us a chance to study the focus while it was still accessible.

Despite all our efforts, if the laser runs continuosly at 200 W the effects on the trapping beam are devastating, as can be seen in figure 3.6. Fortunately it takes some tens of milliseconds until the lensing causes strong distortions of the beam, which gives us a chance to make use of the full laser power during the transfer (see section 4.1).

3.3.3 Time-averaged dipole trapping

To dynamically shape the form of our trapping potential we can modulate the frequency of the sound wave inside two crossed AOMs, which causes the deflection angle of the beam to change. In the first lens of the expansion telescope, which is placed such that its focal plane lies between the two AOMs, the beam is made paraxial again with a position shift $d_{\mathrm{col}} \approx f \cdot \sin\alpha$. This position shift is reconverted into an angle at the collimating lens of the telescope, but the deviation is reduced by the magnification factor of the telescope. The position shift in the fo-

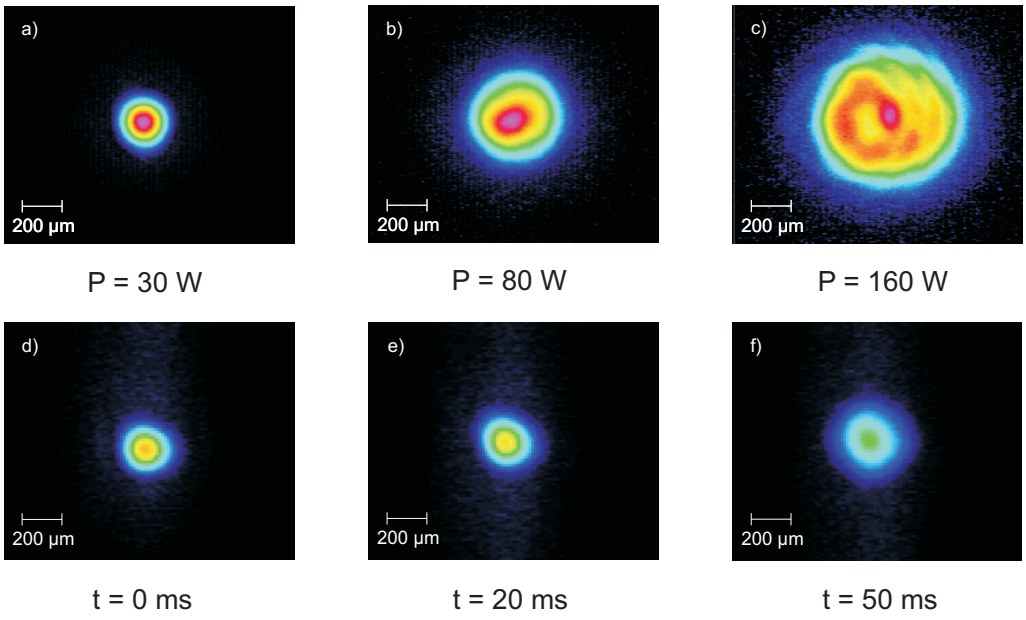

Figure 3.6: Effects of thermal lensing on the focus of the trapping beam. Figures a) to c) show the focus in continous operation at different laser powers. One can see that at low power the beam is an almost perfect gaussian with beam waists $\omega_{\mathrm{x}} = 79\,\mu\mathrm{m}$ and $\omega_{\mathrm{y}} = 81\,\mu\mathrm{m}$, which gets distorted and enlarged to $\omega \approx 155\,\mu\mathrm{m}$ at 130 W. At maximum power the beam shows strong aberrations and is enlarged further to a diameter of $500\,\mu\mathrm{m}$. One should note that when image c) was taken there was some dirt on the optics. Since cleaning the optics and beginning to use a flowbox to keep the air over the optical table clean when the laser is running we have not been able to reproduce such strong abberations.
The bottom figures show how thermal lenses develop over time. Image d) was taken right after the laser was ramped up to its maximium power. One can see the beam still looks good after twenty milliseconds, but in image f), which was taken after 50 ms at maximum power, the beam size has increased to $\omega \approx 120\,\mu\mathrm{m}$. So we can use the maximum power only for about 30ms before the shape of the trap starts to degrade.

cal plane is then $d_\mathrm{f} = (f_1/f_2) f_3 \alpha$ [25]. Expressing this in terms of the beam waist and the size of the beam in the AOM one finds that

$$\frac{d}{\omega_0} = \frac{\alpha\, \omega_{\mathrm{AOM}}}{\lambda} = \epsilon, \tag{3.13}$$

which means that the maximum shift of the focus (given in beam waists) only depends on the beam size in the AOMs and the maximum deflection angle. So we can increase the diameter of our trap by a fixed factor ϵ independent of the diameter of the focus.

The two AOMs (Crystal Technologies, models 3110-197 and -191) in the optical dipole setup have a center frequency of 110 MHz at a Bragg angle of 27.8 mrad and an active aperture of 1.3 mm resp. 1.75 mm. Their frequency range is $\pm 5\mathrm{MHz}$, so the angle deviation of each AOM can be scanned by $\alpha = \pm 1.3\mathrm{mrad}$. Using a scanning range of $2.5\mathrm{mrad}$ and a beam diameter in the AOM of 1.2 mm one obtains a value of $\epsilon = 2.8$, with the diffration efficiency dropping to about 90% of its initial value at maximum deflection. This leads to a nearly box-shaped trap with a maximum size of $225\,\mu\mathrm{m}$ and a depth of $360\,\mu\mathrm{K}$ at maximum power.

To make sure the atoms see a time-averaged potential the scanning of the focus has to happen much faster than the trap frequencies. The AOMs have a specified bandwidth for frequency modulation of $\sim 2.5\mathrm{MHz}$. Their RF-power comes from two VCOs (V110ME01-LF, 100 - 120 MHz, Z-Communications) with 5W amplifiers (ZHL-03-5WF, MiniCircuits). The frequency of these VCOs can be modulated with a modulation frequency larger than 10 MHz via their control input, thus changing the deflection angle of the AOM and consequently the position of the focus. When doing this kind of modulation, one has to ensure that no correlations exist that cause uneven distribution of power, or oscillations at low frequencies. An example for this would be the Lissajou figures that appear when one superimposes two sine wave with slightly different frequencies.

We considered two different approaches to solve this problem. The first one was to apply a DC offset voltage corresponding to 110 MHz and white noise, whose amplitude would then correspond to the maximum frequency shift and therefore the trap size. To avoid correlations between the two AOMs both signals have to come from separate sources. We discarded the idea, because while it would succeed in making the trap larger, we would have no well-defined trap shape.

We chose the opposite way to solve this problem, taking complete control by using two phase locked signals. Two arbitrary waveform generators (Agilent 33220A), which can be phase stabilzed to each other give out arbitrary waveforms which cause the beams to rotate around the center at constant velocity with growing radius. The amplitude of the signal can be altered using a control voltage on the input for external amplitude modulation of the waveform generators, which makes them easy to integrate in our experiment control.

3.4 Feshbach coils

To tune the scattering length we need an additional set of magnetic field coils, which have to be able to produce fields of $B \approx 760\,\mathrm{G}$ with a duty cycle of about 75% for the evaporative cooling towards a BEC and can be ramped to fields in excess of $1400\,\mathrm{G}$ for a short time to do experiments on the BCS side of the resonance. Additionally we want the field to be as homogenous as possible to guarantee an equal scattering length over the entire trap and to avoid distortions of the trapping potential by magnetic field gradients. Minimizing the inductance of the coils to enable fast switching is desireable as well, as the speed of ramps across the Feshbach resonance is a critical parameter in many experiments. A further important consideration was to design our coils to be as simple, robust and easy to build as possible.

3.4.1 Coil design and technical challenges

To get a homogeneous field in the center the geometry of the coils has to stay close to a Helmholtz configuration, where the distance b of the coils is equal to their radius r, so one has to choose between placing small coils close to the atoms, or large ones farther away. As the field strength in the center scales with $1/b$ large coils require more windings or more current for the same field, which leads to larger power supplies and higher cost. Additionally, in our setup the fields of a larger coil would neccessarily pass through the octagon, so abrupt changes in the field would cause eddy currents, limiting the ramping speed.

Therefore we chose to place our Feshbach coils inside the reentrant viewports around our main windows, which is the closest we can get to our atoms (see fig. 3.1). Obviously the available space in this place is very limited, so we use the whole area for a 5 mm thick coil consisting of fifteen windings of flat copper wire with a thickness of 1 mm. The windings are held together by a filled epoxy (Stycast 2762FT, Emerson & Cuming).

To produce the field of $B \approx 760\,\mathrm{G}$ for evaporation a current of $205\,\mathrm{A}$ is needed as shown in fig. 3.7.

At this current the power dissipated in the coils is $P \approx 700\,\mathrm{W}$ which increases to $P \approx 2600\,\mathrm{W}$ at the maximum current of our power supply of $I_{\max} = 400\,\mathrm{A}$, so the coils require very effective cooling. For this we designed water cooled copper heat sinks, which sit on top of the coils. The temperature difference across 5 mm of copper at a power of $2500\,\mathrm{W}$ is less than $5\,\mathrm{K}$, so the critical part for this cooling scheme is the thermal interface between coil and cooler. At first we estimated a temperature difference of

$$\Delta T = \frac{d}{A\sigma} P = 36\,\mathrm{K} \tag{3.14}$$

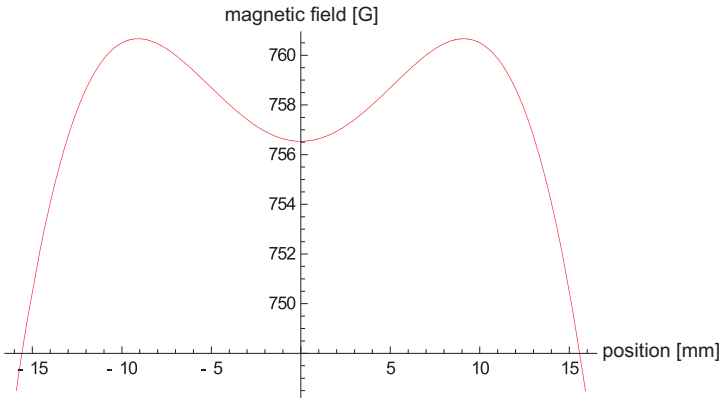

Figure 3.7: Axial magnetic field of our feshbach coils calculated for a distance $b = 30,8\,\mathrm{mm}$ and a current $I = 205\,\mathrm{A}$, which leads to a field of $B = 756\,\mathrm{G}$ with an inhomogenity of less than $20\,\mathrm{mG}$ over $\pm 0.5\,\mathrm{mm}$ around the center.

assuming a layer of Stycast ($\sigma = 1.4\,\frac{W}{m\,K}$) with a thickness of $d = 0.1\,\mathrm{mm}$ at a power of $2500\,\mathrm{W}$ and a coil surface of $A = 50\,\mathrm{cm}^2$. This would lead to a coil temperature of about 55°C, which we considered to be acceptable.

Unfortunately these numbers turned out to be diffult to achieve in practice for several reasons: As the flat wire we use for the coils is rounded at top and bottom and the isolation has bad heat conductivity, the top of the coil must be machined off to get a flat copper surface which can be glued to the heat sink with a suffi-cently thin layer of epoxy. This of course introduces the danger of short circuits between heat sink and coil, which render a coil unusable, so the epoxy has to be thick enough to guarantee electric isolation. As the sapphire filling of the Stycast quickly dulls the tools used for machining the surfaces, our workshop had trouble getting the surfaces flatter than $0.1\mathrm{mm}$, which forced us to use a thicker layer of epoxy. Additionally the used epoxy has a large viscosity, which causes further problems as air is easily entrapped when placing the coil on the heat sink.

Due to these diffculties our first test coil overheated and blew up at a curent of $I_{\max} = 220\,\mathrm{A}$, but the experience gained during the manufacture convinced us that the design had the potential to fulfill our requirements. We therefore built two more coils using the same design, which we currently use in our experiment.

3.4.2 Performance of the Feshbach coils

After completing our coils we first measured the temperature at the bottom of the coils for different currents using an infrared thermometer (Voltcraft IR-1001A). We noticed an inhomogenity of the temperature by a factor of two between the hottest and coldest areas of both coils (see figure 3.8), which is probably due to

localized disruptions of the thermal interface, most likely caused by air bubbles or bad contact between copper and epoxy.

The maximum rated operating temperatures of the wire and the Stycast are 200°C, so to be on the safe side we limit ourselves to a maximum temperature of the coils of $T_{\max} = 100\,^{\circ}\mathrm{C}$. Under this condition the maximum continous current we can apply to our Feshbach coils is $I_{\max} = 215\,\mathrm{A}$. If we run our coils at $I = 205\,\mathrm{A}$ for three seconds we have enough reserve to quickly increase the current to $I = 400\,\mathrm{A}$ for 100 ms if we switch off the current for 900ms afterwards, which is a good approximation for our expected experimental cycle of a one second long phase of MOT loading, followed by three seconds of evaporation and about 100ms for the actual experiment.

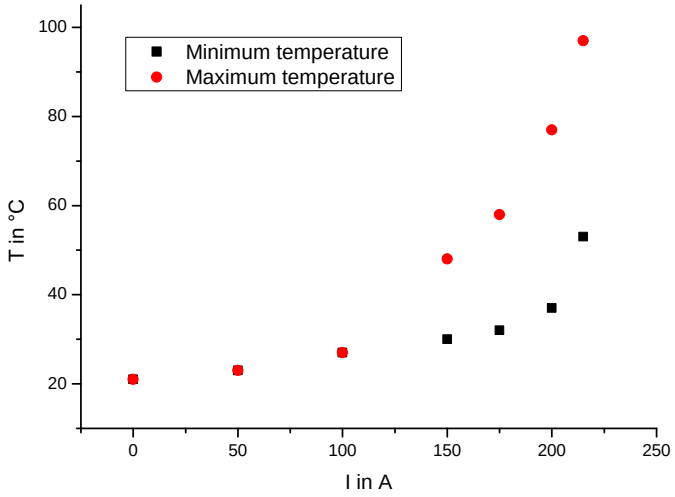

Figure 3.8: Temperature of the upper feshbach coil in continous operation for a hot and cold spot of the coil. The average temperature at $I = 215\,\mathrm{A}$ is approximately ten degrees above the lower limit.

To verify our simulation of the magnetic field and test our mounting scheme we placed the coils in aluminum models of our reentrant viewports and set them up in a distance of $d = 31 \pm 0.1\,\mathrm{mm}$. As the resolution of the hall probe we used was on the order of one Gauss we could only verify the strength and not the shape of the magnetic field. The measured value of $B = 734 \pm 1\,\mathrm{G}$ in the center at $I = 200\,\mathrm{A}$ agrees with the theoretical value within the error of positioning and the resolution of the probe.

A more detailed examination of the field in the trapping region will be possible through RF spectroscopy of the atoms as soon as the neccessary hardware has

been implemented.

To stabilize the magnetic field we use a current transducer (Ultrastab 688, Danfysik) and a precision resistor to measure the current through the coils. The resulting voltage is amplified and fed into our real-time experiment control (see section 3.5) where it is used as an error signal for a digital PID controller. With this system we achieve a relative stability of the current better than 10^{-4}.

When ramping the magnetic field we can ramp up from zero current to $I = 200\,\mathrm{A}$ in $1.2\,\mathrm{ms}$ and from there across the resonance to $I = 400\,\mathrm{A}$ in about $2.2\,\mathrm{ms}$, while the way back from $I = 400\,\mathrm{A}$ to $I = 200\,\mathrm{A}$ takes about $1.6\,\mathrm{ms}$.

While our coils should be sufficent for the experiments we are planning to do at the moment, we would prefer coils which allow longer hold times at magnetic fields $> 800\,\mathrm{G}$ and do not heat our vacuum chamber as much, as this can limit the trap lifetimes of our atoms.

By using an unfilled epoxy for the coil and using materials designed for the connection of processor dies with their heatspreaders we hope to improve the thermal interface between coil and heat sink by at least a factor of 4, which would allow continous operation of the coils at $I = 400\,\mathrm{A}$ and reduce coil temperature to about 30°C at $I = 200\,\mathrm{A}$.

3.5 Experiment control

The experiment is controlled by an independent real-time system (ADwin Pro II, Jäger Messtechnik) with eight 16-bit analog outputs, eight 18-bit analog inputs and 32 digital I/O channels. Due to the modular structure of the systems additional in- and outputs can be added as needed.

The system contains a DSP processor, which continually executes real-time processes with a fixed runtime t_p. We employ a single high priority process which can update the state of all analog and digital outputs at the same time, according to a table containing all timing events for one experimental cycle. The process can complete all tasks in a runtime of $t_\mathrm{p} = 10\,\mu\mathrm{s}$ which allows to set the outputs with a bandwidth of 100 kHz.

The value of the analog outputs can either be set directly or stabilized to a signal provided on one of the analog inputs via a digital feedback loop, which is part of the real-time process running on the ADwin system. The regulation parameters can be set to any value in the ADbasic program. This way we do not have to design an analog controller for every feedback loop we wish to add to our experiment, but can simply set up a detector to provide a reference signal and plug it into the experiment control.

The user interface is provided by a Labview program. It displays the experimental cycle divided into independent subsequences, which can be timed relative to

each other. These sequences contain the digital and analog events, with timings given relative to the start of their sequence. All timings and output values can be entered either directly, or as formulas containing user defined variables, which greatly enhances clarity. From this timing array the Labview program creates the timing table for the ADwin, writes it to its memory via a LAN connection, and starts the experimental cycle.

To automatize the experiment it is possible to set the Labview program to continously run the experiment while tuning one or more variables over a given range, employing a user defined parameterization.

To ease the evaluation of the collected data the values of all variables are sent to the Labview program controlling the camera during each run of the experiment, which saves them into a spreadsheet file, together with the temperatures and particle numbers extracted from the absorption images.

Chapter 4

Evaporative cooling of Lithium

This chapter gives an account of the first measurements performed to test our magnetic field coils and characterize our crossed beam dipole trap.

After overlapping the infrared beams and optimizing the transfer into the dipole trap, we started by calibrating our magnetic field and got good agreement with the simulations done when planning the coils. The measurement of trap frequencies proved to be more difficult, as the trap shape is not well defined even at medium power. Measurements taken at low power gave better results, but they differ strongly from the properties we calculated before setting up the trap. Although we spent quite some time looking for the reason, we have not found a consistent explanation for this difference so far.

Additionally the lifetime of the atoms in our trap is rather short, but this will probably be improved as soon as intensity stabilization can be implemented.

All measurements discussed in this section were done in random order, using the automization feature of our experiment control to minimize the effects of slow drifts of the system. As in most measurements the differences between the data points are more important than their absolute values, the error bars in the plots denote the statistical error of the measurements, while systematic errors are discussed seperately.

4.1 Loading of the crossed dipole trap

4.1.1 Preparing the MOT for transfer

To get optimum starting conditions for evaporative cooling we need the MOT to be as cold and dense as possible during the transfer (see eqn. 2.31). To achieve this we have to ramp the laser detuning close to resonance, as the minimum temperature and maximum confinement are reached at a detuning of $\delta = -\Gamma/2$. To avoid

power broadening of the transition and reduce losses through light asissted collisions, which scale with the square of the density, we have to lower the laser power at the same time. The maximum density is reached when the light pressures from the cooling beams and reabsorption of scatterd photons are in equlibrium. This is called the density limited regime, where the volume of the MOT grows linearly with the particle number.

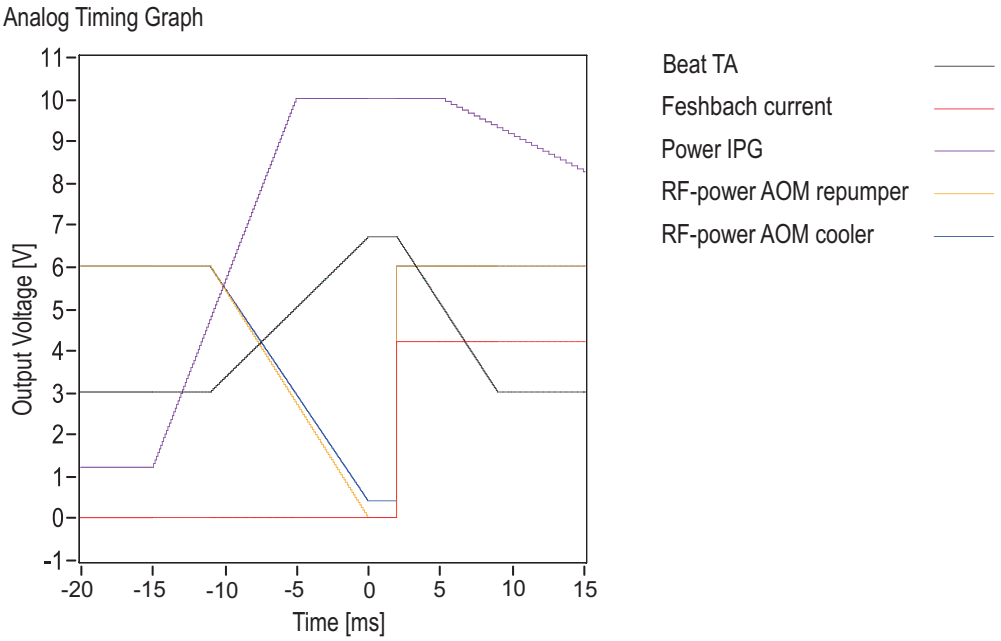

Figure 4.1: Values of the relevant analog outputs of the experiment control during the transfer.

During the optimization of the transfer it proved useful to time all events relative to the point the MOT light is turned off by cutting the radio-frequecy (RF) power to the AOMs with RF switches (ZASWA-2-50DR+, MiniCircuits). We define this as the point of transfer at $t = 0$.

The first step is to switch off the laser and magnetic field coils of the Zeeman slower at $t = -100\,\mathrm{ms}$ to elimininate their influence on the position of the MOT. The actual transfer procedure (see fig. 4.1) starts at $t = -15\,\mathrm{ms}$ by ramping up the power of the fiber laser from its minimum value of ~10 W to its maximum power over $10\,\mathrm{ms}$. We keep this time short to reduce thermal effects caused by the high power beam (see fig. 3.6).

At $t = -12\,\mathrm{ms}$ we start the intensity and detuning ramps to compress and cool the MOT. We ramp the detuning from its loading value of $\delta_{\mathrm{load}} = -7\,\Gamma$ to $\delta_{\mathrm{min}} = -1.2\,\Gamma$ at $t = 0$. This detuning is far larger than the theoretical optimum for

cooling, but the number of transferred particles drops significantly at values of $\delta_{\min} > -1\Gamma$. To reduce the laser power we apply linear ramps to the control voltages of the RF drivers of the AOMs. Optical pumping from the $F = \frac{3}{2}$ to the $F = \frac{1}{2}$ state, which is stable against inelastic decay in the dipole trap, is achieved by ramping down the repumper a little faster than the cooler. At the end of the ramps the MOT is compressed to a diameter of $d \approx 600\,\mu\mathrm{m}$, containing $1.2 \cdot 10^7$ atoms at a temperature of $T \approx 250\mu\mathrm{K}$, which according to

$$\rho = \lambda_{th}^3 n = \left(\frac{h^2}{2\pi m k_\mathrm{b} T}\right)^{\frac{3}{2}} n \tag{4.1}$$

gives an estimated phase space density of

$$\rho_{\mathrm{MOT}} \approx 8 \cdot 10^{-6}. \tag{4.2}$$

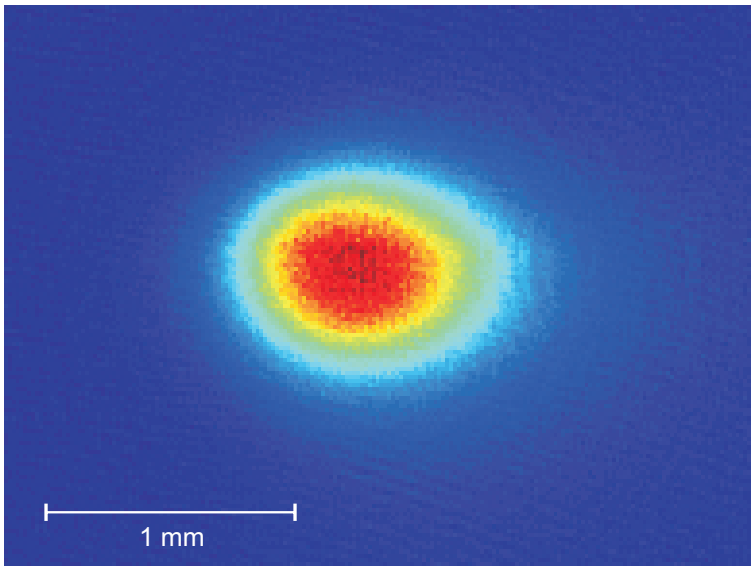

Figure 4.2: Absorption image of the MOT at $t = 0$ taken to determine particle number and diameter. By taking an image after a time of flight we can also measure the temperature of the MOT at the point of transfer.

At the transfer point $t = 0$ we close the RF switches and cut off the curent in the MOT coils with four parallel MOSFETs protected against induction voltages by varistors. The current subsides in only $3\,\mathrm{ms}$, but due to eddy currents in the octagon the magnetic field does not vanish completely for about $100\,\mathrm{ms}$. Mechanical shutters made from loudspeakers block the cooler and repumper beams a few ms after the transfer, the RF-power for the AOMs is ramped up again and $10\,\mathrm{ms}$ after the transfer the RF-switches are opened. This is necessary to avoid thermal drifts in the AOMs.

4.1.2 Adjusting the optical dipole trap

As we had already developed a transfer procedure for preliminary experiments conducted in the quadrupole trap provided by the MOT field and a single beam dipole trap we only had to optimize the spatial overlap of the two infrared beams. We did the rough adjustment of the beam path with the breadboard holding the optics placed on a technical drawing of the vacuum setup.

After moving the breadboard in place it was easy to use resonant laser beams to blow away the MOT and overlap the infrared beams with them. This gave us a sufficent overlap to detect the beams via absorption imaging and use the images to optimize their position. For the vertical axis and the horizontal axis perpendicular to the viewing direction this was straightforward, but in the viewing axis the images give little information about the overlap of the crossing point with the MOT.

Fortunately even a single beam forms a trap at full power, which allows us to block the returning beam and adjust the position of the incoming beam in the viewing axis by maximizing the atom number after recapture in the MOT. If we tune the overlap using only the position of the returning beam we can be fairly certain that the beams cross in the center of the MOT.

This procedure could be simplified if the beams had a smaller waist of about $60\,\mu\mathrm{m}$, which would result in a shorter Rayleigh range and hence a decent longitudinal confinement for the single beams. We therefore intend to decrease the size of the foci in the near future.

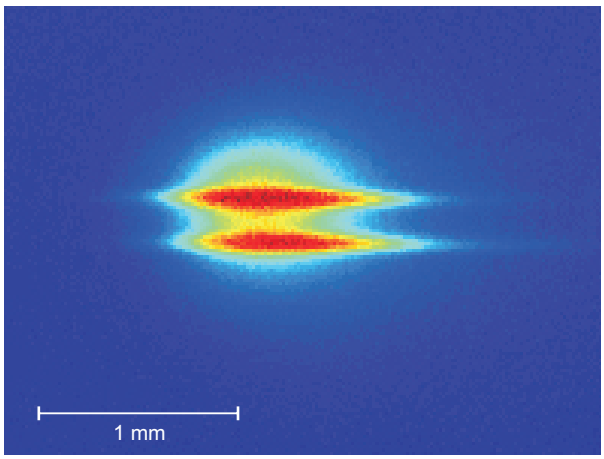

Figure 4.3: Absorption image of the transfer at $t = 0$. While both beams already hit the MOT they still have to be overlapped in the vertical direction.

4.1.3 Transfer efficiency

When we first tried to measure the transfer efficency we noticed a strong discrepancy between the values obtained with absorbtion and fluoresescence measurements. While an absorbtion picture would show only $1.2 \cdot 10^6$ atoms after $10\,\mathrm{ms}$ and $8 \cdot 10^5$ atoms after $100\,\mathrm{ms}$, recapturing the atoms in the MOT and measuring the fluorescence after $100\,\mathrm{ms}$ returned a value of $4.75 \cdot 10^6$ particles. The values measured for the MOT are $1.2 \cdot 10^7$ and $1.35 \cdot 10^7$ respectively and agree very well within the accuracy of the measurements. The possibilty of magnetic trapping significantly altering the result was excluded by doing a fluoresence measurement without the dipole trap, which found only 60000 atoms after 100 ms.

The explanation for this surprising difference is that about three quarters of the atoms are not captured in the crossed trap and leave along the laser beams (see fig. 4.4). But as the foci of the beams are tight enough to provide a longitudinal confinement with a trap frequency of $\omega_\mathrm{s} = 13\,\mathrm{Hz}$ at this power, these atoms are not completely lost but remain trapped in the arms.

This separation of our trap into two parts makes it difficult to rate the success of our transfer, as the atoms captured in the center are packed denser and are therefore more valuable than the ones in the very shallow traps outside. For the part of the sample captured in the crossed region particle number and temperature are easy to measure with absorption imaging, which yields values of $N_\mathrm{abs} = 1 \cdot 10^6$ and $T \approx 240\,\mu\mathrm{K}$ for $t = 10\,\mathrm{ms}$ after transfer. The number of particles in the arms of the trap can be obtained by subtracting N_abs from the value measured via fluorescence imaging, but their temperature can not be measured as density is too low to get an absorption signal after a time of flight. We will see in the next section that the situation is still highly dynamic at this point, so we will refrain from doing a full analysis of this state of the system.

4.1.4 First stage of forced evaporation

As the truncation parameter is usually low right after transfer, the usual procedure in all-optical BEC experiments is to just hold the atoms until plain evaporation stagnates. This minimizes particle loss until evaporation has reached its highest possible efficiency.

Unfortunately we cannot do this with our current setup, because we have only about $30\,\mathrm{ms}$ at maximum laser power before the focus gets significantly enlarged by thermal effects in the optics (see fig. 3.6). In absorption images of the trap an additional problem which we had not noticed before became visible: Over a time of several hundred miliseconds to a few seconds the vertical positions of the beams move by several hundred micrometers, until the overlap is almost lost (see fig. 4.5). As this depends on the laser power we assume it is another thermal

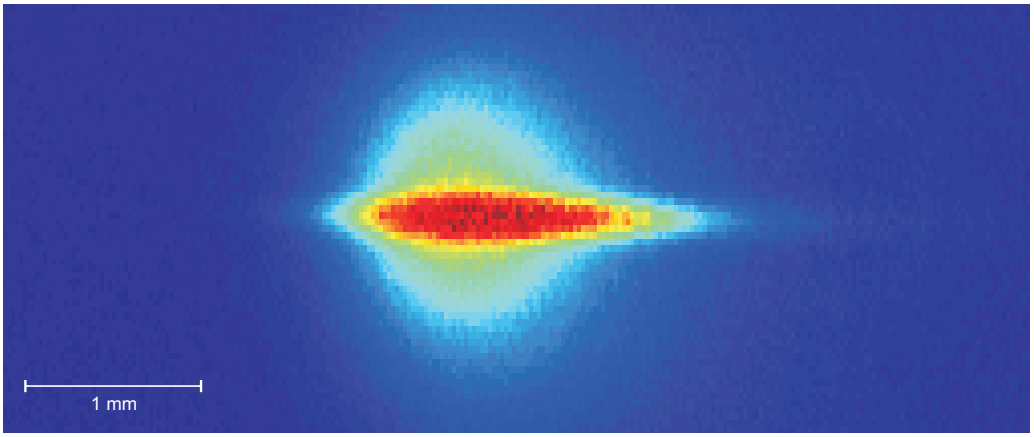

t = 0 ms

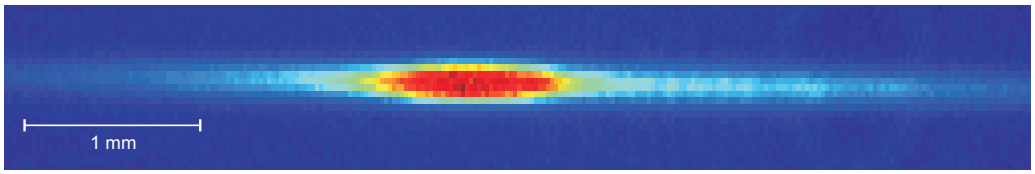

t = 2 ms

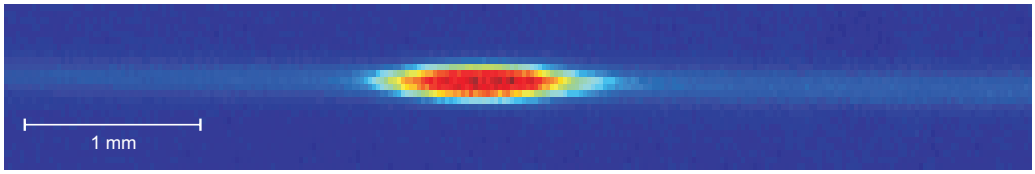

t = 5 ms

Figure 4.4: Absorption images of the dipole trap for different times after transfer. A large part of the atoms initially captured from the MOT leaves the crossing region and escapes into the tubes formed by the laser beams.

effect, but the exact source has not been found yet.

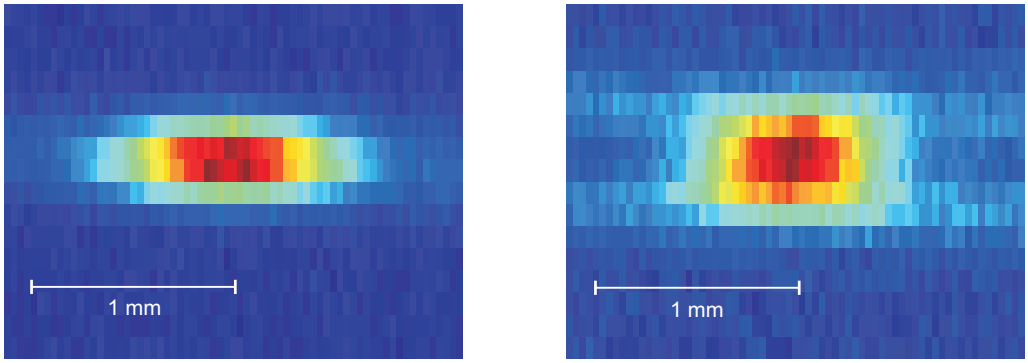

Figure 4.5: Separation of the dipole trap after one second. One can clearly see that the trap degrades faster at higher laser power.

As a rapid decrease in trap depth is unavoidable, we try to make the best of the situation by switching on the interactions only $2\,\mathrm{ms}$ after the transfer. By ramping up the current in our Feshbach coils to $210\,\mathrm{A}$ over $1.2\,\mathrm{ms}$, which corresponds to a homogeneous magnetic field of $755\,\mathrm{G}$, we try to turn what would be a spilling of atoms from the trap at zero field into - unfortunately not very efficent - evaporative cooling.

The problem caused by the uncontrolled broadening of the focus is not the reduced trap depth, as this is compensated through adiabatic cooling, but that the trap frequencies drop with $\bar{\omega} \propto \omega_0^2$, which dramatically decreases the density $n \propto \bar{a}_{\mathrm{ho}}^3 \propto \bar{\omega}^{\frac{3}{2}}$ and therefore the rate of elastic collisions, making evaporation even less efficient.

To keep thermal effects to a miminmum we keep the power of the fiber laser at the smallest stable value as long as possible before ramping to maximum power five milliseconds before the transfer. We keep it at the maximum for another five milliseconds after the transfer, just long enough to switch the magnetic field to 755 G. Afterwards we ramp the laser down over 40 ms to a holding value below 100 W where we have more stable conditions.

We believe that the cooling during the ramp is mostly adiabatic due to its high speed, as the number of particles remaining after plain evaporation decreases only by about twenty percent if we leave the magnetic field switched off during the ramp. But as we cannot measure trap frequencies at full power, and the trap shape evolves during the ramp, we cannot give a quantitative analysis at the moment.

This procedure is highly inefficient, as we loose about two thirds of the particles through the decrease in trap depth with no or very little gain in phase space density.

First attempts to improve the transfer through time averaging of the dipole trap had little success, so we decided to first do a proper characterization of the static trap before continuing in this direction.

4.2 Tuning the interactions

To get confirmation that our magnetic field coils were working correctly we did a quick measurement of particle loss from our dipole trap versus the current in our Feshbach coils (see fig. 4.6). We did this by transferring the atoms into our dipole trap and ramping down the laser power to 37 W in 40 milliseconds, followed by holding the atoms at the probe field for $1\,\mathrm{s}$. Afterwards we measured the number of remaining atoms by switching off the magnetic field and recapturing them in the MOT. This measurement gives an indication for the value of the scattering length by the amount of evaporative loss which is observed [26].

From this we got a rough estimate for the current corresponding to the zero crossing of the scattering length at $534\,\mathrm{G}$ of $145 \pm 5\,\mathrm{A}$, which agreed well with our simulations. But additionally we found a strong loss feature close to zero magnetic field which cannot be explained by the known behavior of the scattering length. A more detailed scan of the region located the maximum loss at $19 \pm 8\,\mathrm{G}$, with a measured width of about $15\,\mathrm{G}$.

As we could not explain this phenomenon, we decided to do a more thorough calibration of the magnetic field. We took absorption images at different magnetic fields, measuring the detunings of the imaging laser which corresponded to the maximum in the cross section with a spectrum analyzer.

Imaging at a current of $0\,\mathrm{A}$ showed the magnetic sublevels to be degenerate, with a detuning of the imaging laser of $228 \pm 1\,\mathrm{MHz}$ to the frequency reference laser locked to the $F = 3/2$ transition, which matches a field of $0 \pm 3\,\mathrm{G}$.

At a current of $210\,\mathrm{A}$ we measured an optimal detuning of $1056 \pm 1\,MHz$, corresponding to a Zeeman shift of $1204 \pm 2\,\mathrm{MHz}$ for the

$$|S_{\frac{1}{2}}, m_\mathrm{s} = -\frac{1}{2}\rangle \rightarrow |P_{\frac{3}{2}}, m_\mathrm{j} = -\frac{3}{2}\rangle$$

transition. Comparing this to the theoretical value sets the magnetic field to $755 \pm 1.4\,\mathrm{G}$, which is in excellent agreement with the simulations (see fig. 3.7).

Although our magnetic field coils work as intended, there is still a strong likelihood of a technical reason for the observed loss feature. Therefore we did not spend time on a more thorough investigation at this time, but we intend to look at this again when we have a more detailed understanding of our setup.

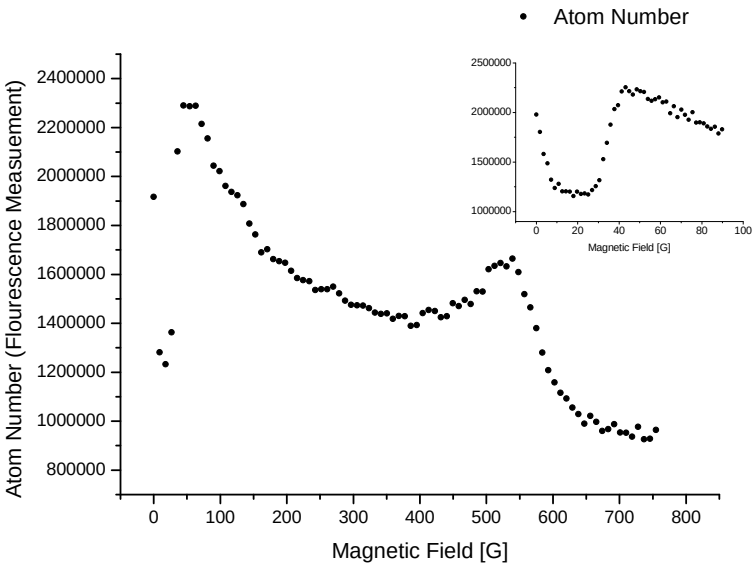

Figure 4.6: Losses from the optical dipole trap for different values of the magnetic field. The zero crossing of the scattering length at 534 G is clearly visible. The strong losses at low field (see insert) could come from a previously overlooked resonance phenomenon or unknown technical reasons. Due to the extensive studies which have been conducted on the scattering properties Li_6 in the past, as for example in [27], we currently favor the second hypothesis.

4.3 Plain evaporation

After the initial decrease in trap depth we hold the atoms at a laser power of 32 W in a magnetic field of 755 G for cooling through plain evaporation. To measure the evolution of temperature and particle number we stopped plain evaporation at different times by switching off the magnetic field and taking a time of flight image of the cloud twenty milliseconds later. Taking the images at zero field was possible as the temperature was still high enough that no molecules could be formed, which would not be detected by this imaging technique. The results are plotted in fig 4.7.

While temperature drops steadily until it stagnates after $900\,\mathrm{ms}$, the measured particle number increases by ten percent in the first 500 ms. We believe that atoms in the shallow traps formed by the individual beams scatter when they cross the region of high density in the center of the trap and are cooled into the deeper part of the trap where we can detect them with absorption imaging.

As we took images at zero field the approximation used for the scattering cross section is too simplistic, this probably dominates the error of the measured particle number. To be on the safe side we assume a possible systematic error of 50% for

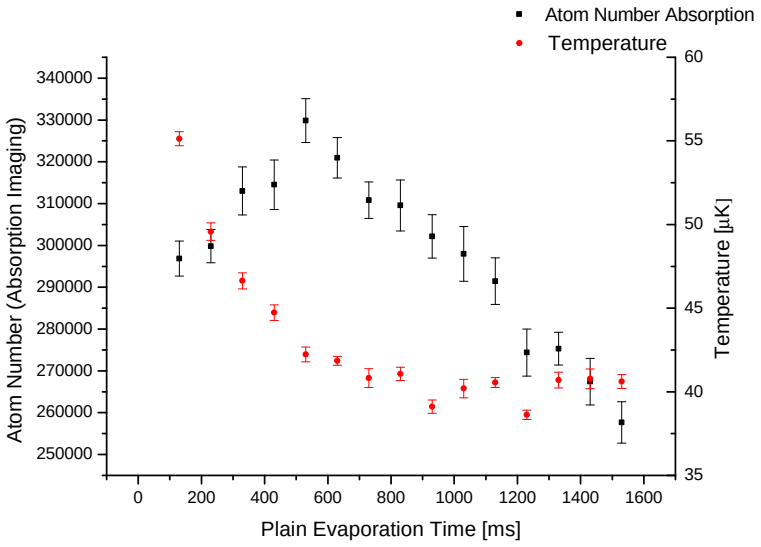

Figure 4.7: Change of particle number and temperature during plain evaporation.

this value in further calculations.

The main diffculty when measuring the temperature is the error in the magnification of the camera. To determine our magnification we varied the frequency of the Y-axis AOM and measured the position shift of the beam with absorption imaging. Comparing it with the movement of the focus in a monitoring setup behind a mirror allowed us to meaure the magnification with an accuracy better than 10 %. Assuming this to be the main source of error we get a temperature at stagnation of $T = 40 \pm 4\,\mu\mathrm{K}$, with $3 \cdot 10^5 \pm 50\%$ remaining particles.

To determine whether these are starting conditions which give us a chance to reach a BEC through forced evaporation, we still need information about the trap frequencies and the lifetime of the atoms in the trap, which will both be adressed in the next section.

4.4 Properties of the dipole trap

4.4.1 Lifetime measurements

To measure the lifetime in the trap we held the atoms after plain evaporation, both with and without magnetic field. Measuring the number of remaining particles and their temperature through absorption imaging we got the results plotted in figure 4.8. We found an exponential decay with a lifetime of $2.5 \pm 0.4\,\mathrm{s}$ for both cases. As we measured lifetimes of more than one minute in our magnetic trap this cannot be explained by collisons with the background gas.

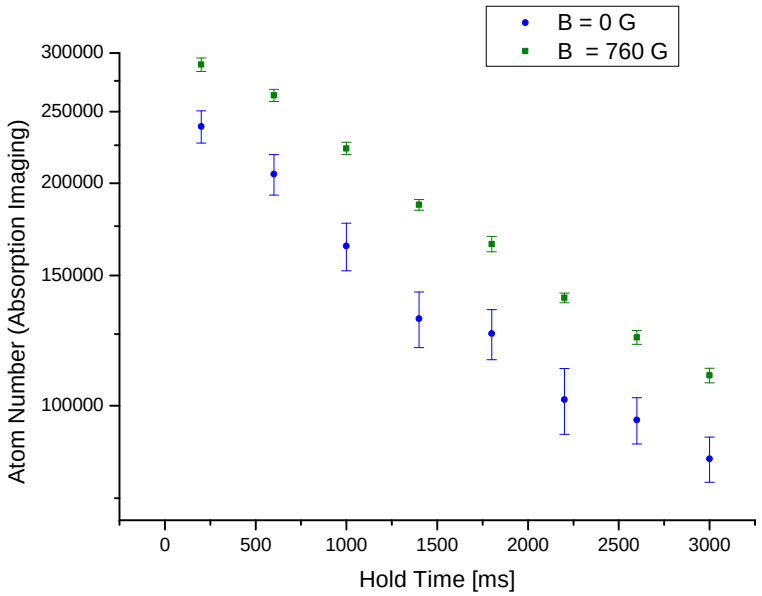

Figure 4.8: Lifetime of the atoms in the crossed beam dipole trap at a laser power of 37 W for different magnetic fields. While the total number of particles measured is slightly lower for the second curve, the lifetimes are almost the same.

If one takes a look at the temperature measurements (see fig. 4.9), one sees that while holding the atoms at zero field the sample is heated by only about $4\,\mu$K per second. As we just completed a phase of plain evaporation the temperature is a lot smaller than the trap depth, so this heating rate cannot explain such strong losses. The fact that temperature slowly increases even when the elastic collisions are turned on can be explained by the decreasing density in the trap, which lowers the cooling rate and shifts the equlibrium to higher temperatures.

As the decay is clearly exponential we believe it to be dominated by a one-body process. A possible candidate could be interactions with the trapping light giving the atoms enough energy to leave the trap at once. As we already measured lifetimes of up to thirty seconds in a single beam trap the effect is probably related to the crossing of the beams. This hypothesis is supported by the fact that the lifetime drops to about 20 ms if we do not cross the polarization of the counter-propagating beams. This gives us hope that we can improve lifetime by inserting a brewster polarizer into the beam to get well-defined polarizations in the trap.

4.4.2 Determining the trap frequencies

One method to measure trap frequencies is to cause losses from the dipole trap by the laser intensity. When scanning the excitation frequency trap loss is reso-

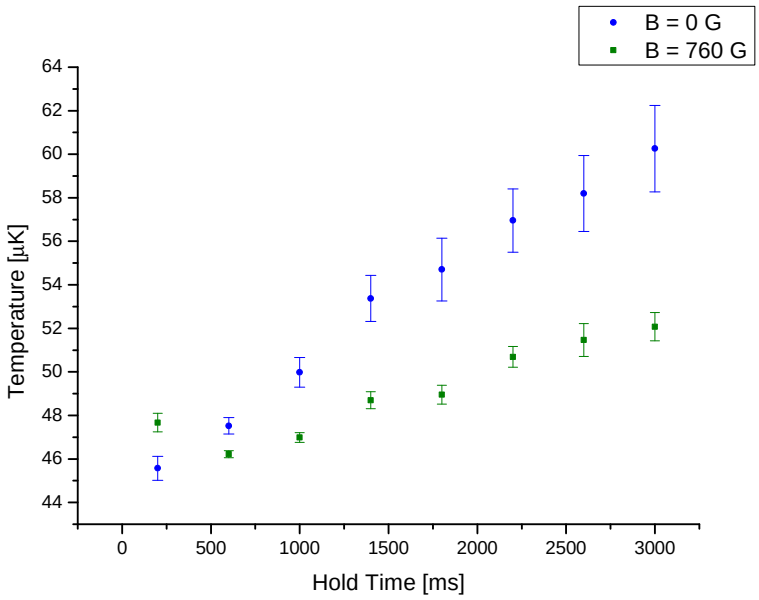

Figure 4.9: Temperature increase after completion of plain evaporation for different magetic fields. As the scattering length of ^{6}Li is almost zero without magnetic field one can assume the particles to be non-interacting and take the increase in temperature as an indication for the heating rate.

nantly enhanced every time the excitation frequency is twice as large as one of the trap frequencies. This can be explained by the following simple picture: If the excitation is twice as large as the trap frequency, the walls of the trap move towards the atoms every time they are at their turning point. This leads to maximum momentum transfer and therefore maximum heating.

As this method is simple and known to give quite reliable results, we used it to determine the trapping frequencies of our setup. We first ramped down the intensity to values where we believed the trap shape to be stable and waited for plain evaporation to stagnate. Then we switched off the interactions by ramping the magnetic field to zero and started modulating a sine wave onto the laser intensity with the analog control input of the laser. We used a fixed number of one hundred oscillations with a modulation depth of about ten percent, waiting afterwards to always take the absorption image at the same time.

Figures 4.11 and 4.10 show scans for the radial and longitudinal trap frequencies at a laser power of $22\,\mathrm{W}$. One can clearly see in the graph showing the scan for the radial frequency that maximum loss and maximum temperature are observed for different excitations.

The reason is that the trap is not completely harmonic; the gaussian shape of the beams leads to a decrease in the trap frequencies seen by atoms close to the edge

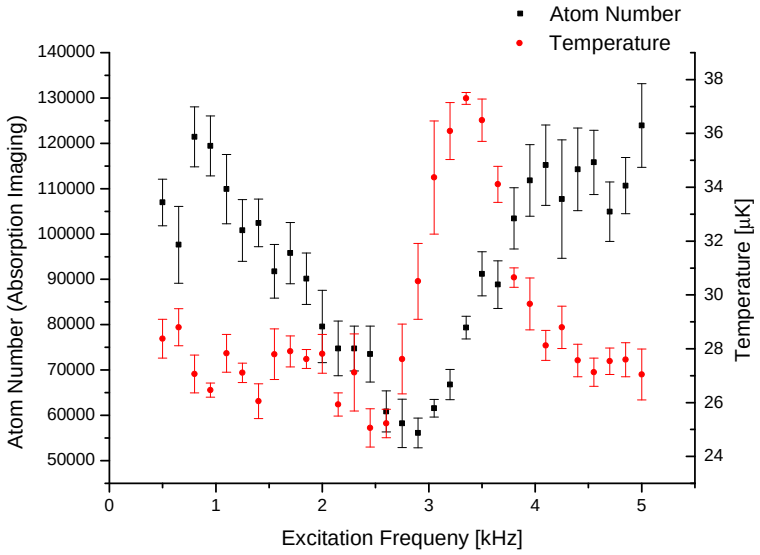

Figure 4.10: Scan through the excitation frequency looking for the radial trap frequency at P = 22 W. The maximum particle loss is shifted down by about 600 Hz relative to the trap frequency determined by the temperature measurement.

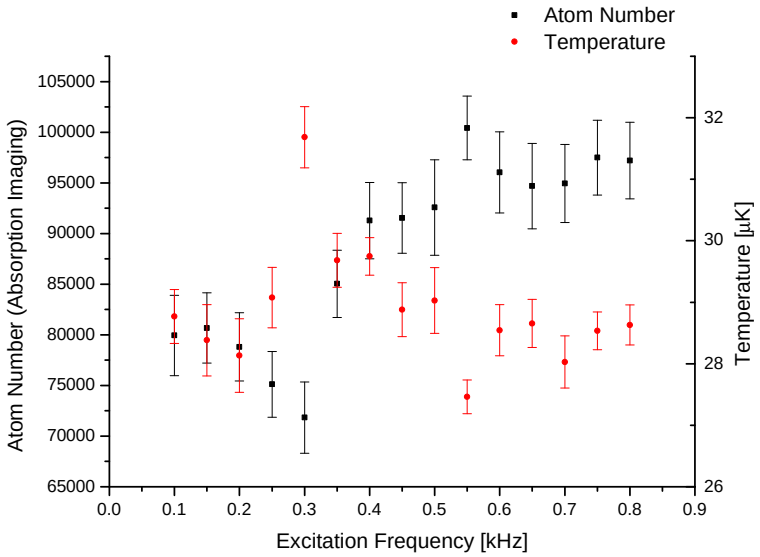

Figure 4.11: In the measurement of the longitudinal frequency we noticed a decrease in losses and heating for an excitation four times the trap frequency. As we see the opposite behavior for a laser power of P = 37 W we believe that this is not an error in the measurement, but a sign of the oscillation coupling to higher modes.

of the trap. Therefore maximum loss occurs when the excitation is slightly below the actual trap frequency, as hot atoms in the high regions of the trap become resonant and are removed from the trap. This causes a systematic downshift when measuring trap frequencies with resonantly enhanced losses.

On the other hand, cold atoms trapped in the center see a harmonic potential and are resonant at exactly twice the trap frequency. But as soon as they are heated they leave the harmonic region and remain trapped with higher temperature. Hence the maximum increase in temperature should be a much more reliable indicator for the actual trap frequency.

Using the temperature measurements to determine the trap frequencies we obtain values of $\omega_r = 2\pi \cdot (1675 \pm 100)\,\mathrm{Hz}$ and $\omega_z = 2\pi \cdot (150 \pm 25)\,\mathrm{Hz}$ for a laser power of $22\,\mathrm{W}$. For $P = 37\,\mathrm{W}$ we get frequencies of $\omega_r = 2\pi \cdot (2200 \pm 100)\,\mathrm{Hz}$ and $\omega_z = 2\pi \cdot (225 \pm 25)\,\mathrm{Hz}$.

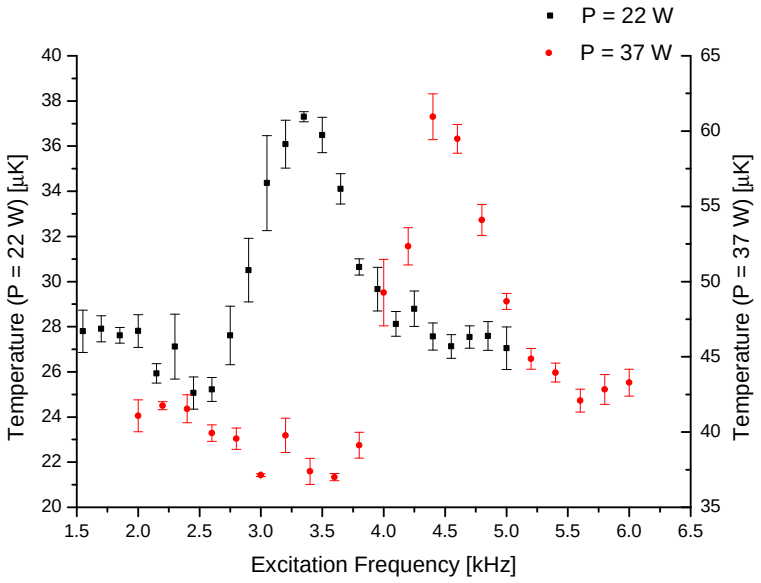

Figure 4.12: Measurement of the radial trap frequency for different trap depths. The good agreement of theoretical and measured values shows that the shape of the trap is stable at laser powers below $P \approx 40\,\mathrm{W}$

As the trap frequencies scale with the square root of the power we expect a ratio of the trap frequencies of $\sqrt{\frac{37\,\mathrm{W}}{22\,\mathrm{W}}} = \frac{\omega_{37}}{\omega_{22}} = 1.30$, which agrees very well with the measured ratio of the radial trap frequencies of 1.31 ± 0.10.

While the measured values are in good agreement with each other, they differ from the values we calculate for the geometry of our setup (see section 3.3.1). The small deviation from the calculated radial frequency of $\omega_r = 2\pi \cdot 1780\,\mathrm{Hz}$ at $P = 22\,\mathrm{W}$ could be explained by a slightly larger focus, but the difference in the

aspect ratio is not so easily explained. The measured longitudinal trap frequency is 30% smaller than the expected value of $\omega_z = 2\pi \cdot 220\,\mathrm{Hz}$, which shifts the aspect ratio from about 8.1 for the calculated shape to $11.1 \pm 2.0.$ and 9.8 ± 1.4 for powers of $22\,\mathrm{W}$ and $37\,\mathrm{W}$ respectively.

So far we have not been able to find a good explanation for this. But changing the size of the foci to $\omega_0 = 60\,\mu\mathrm{m}$ should enable us to trap atoms in the single beams and characterize these traps individually with the methods we established probing our crossed dipole trap. Afterwards we can overlap the individual traps, the only degrees of freedom being crossing position and angle, which we could then infer from the frequencies measured for the combined trap.

4.5 Starting conditions for forced evaporation

Knowing the trap frequencies we can now plot the gain in phase space density during the plain evaporation:

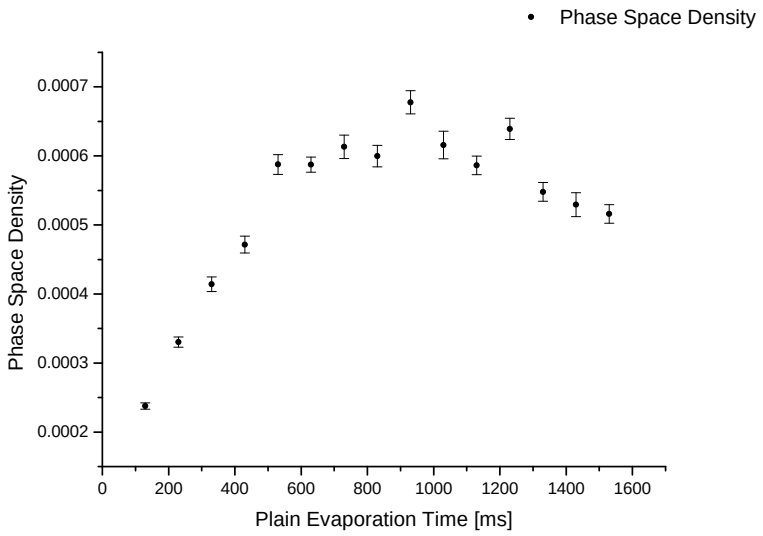

Figure 4.13: Increase of the phase space density during plain evaporation. We reach the maximum phase space density of $6 \cdot 10^{-4}$ after $500\,\mathrm{ms}$.

From this plot we can see that we reach the maximum phase space density of $(6 \pm 3) \cdot 10^{-4}$ after $500\,\mathrm{ms}$ of plain evaporation, an improvement by two orders of magnitude compared to the phase space density of the MOT. But this value is still quite low when compared to the trap frequencies and the short lifetime of $2.5\,\mathrm{s}$, which makes these starting conditions insufficient for reaching Bose-Einstein condensation through forced evaporation.

Therefore the next steps we take will be aimed at improving these starting conditions. The first thing to do will be to use smaller foci to get better control over the trapping conditions, and increase the axial trap frequency for the atoms captured in the arms of the trap. As soon as we have a good understanding of the trap we can use the time averaging to dynamically decrease the volume of our trap, making it possible to increase density right after transfer and hopefully make the first stage of forced evaporation more efficient. Thus we could reach a stable trap without discarding most of the atoms during the ramp.

Furthermore we are planning a MOSFET array which can switch the Feshbach coils to an anti-Helmholtz configuration, which would give us the option to use them as MOT coils in the final stage of the transfer. This would allow us to increase the density of the MOT during the transfer by using a stronger magnetic field gradient, hopefully further increasing the number of atoms we can load into our dipole trap.

We are confident that when all these things have been implemented we will be able to produce our first molecular BEC.

Chapter 5

Conclusion and Outlook

The ultracold quantum gases group at the MPI for nuclear physics was founded in October 2006 with the appointment of Juniorprofessor Selim Jochim, who was joined by his first diploma student Friedhelm Serwane on the first day. From October to January they planned the vacuum setup and the magnetic field coils, ordered the lasers and a supply of optics, and transformed a storeroom into a lab. In January things were far enough along that the actual build-up could start, and Timo Ottenstein and I joined the team.

We initially focussed on assembling the vacuum chamber, spending the remaining time with the MOT lasers. The oven chamber was assembled and baked out in April, and the main chamber followed 6 weeks later. By then we had the MOT lasers locked and running, and after we had solved some minor problems with the cooling of our MOT and Zeemann slower coils we could proceed to set up the outcouplers for the MOT light around the chamber. We had our first MOT the same night, although it was small and took forever to load.

But after some days of nurturing our MOT grew out of its infancy, and as soon as the experiment control was working and the CDD camera was set up for fluorescence imaging we could do a proper optimization and characterization of our MOT.

The next things on the agenda were testing the setup for the dipole trap and building the Feshbach coils. Those two projects proved to be a lot tougher than anticipated, and it took until the middle of December until we had solved the arising problems - or had decided to live with them for the time being. In the meantime we were joined by Matthias Kohnen, who started by doing tests on the generation of arbitrary optical potentials. We practiced the transfer of atoms into a single beam running wave trap to gain some experience for the setup of our crossed dipole trap and did some preliminary measurements of trap lifetime and laser noise.

Two weeks before Christmas we dismantled our MOT and started building the

final version of the dipole trap on a large breadboard, as well as testing the Feshbach coils and installing them into the experiment. In the next week we were ready to move the breadboard over to the experiment, transferring the first atoms into the crossed dipole trap on the last day before the christmas holidays.

When we resumed our work in the new year we quickly managed to optimize the initial transfer, but it took some time to realize the full extent of the thermal drifts and to optimize the second half of the transfer procedure accordingly.

We can currently tansfer $1 \cdot 10^6$ lithium atoms in our crossed dipole trap and create the homogenous magnetic fields needed to tune their interactions. This allows us to increase the phase space density in the trap by two orders of magnitude through plain evaporation, giving us $3 \cdot 10^5$ atoms with a phase space density of $6 \cdot 10^{-4}$.

With the measurements of trap frequencies and lifetimes in the last week we learned a lot about the characteristics of our setup — enough to identify some problems and think of ways to solve them. So while there is still some work to do before we can create our first molecular BEC, we have a good starting position and confidence in the potential of our setup.

While getting our first BEC certainly has a high priority, there are a lot of other things we have to do in the coming months. Although the rough calibration we did of the magnetic field is sufficient for now, improving it will require implementing the tools for RF spectroscopy. To have a chance of spilling our atoms in a controlled way a tight trap with large level spacing is requirded. We already planned a microtrap for this, which will have to be implemented together with the high resolution imaging system. As soon as this trap is available we will need a way to count and finally spatially resolve very small numbers of atoms; although there are some rough ideas there is still a lot of work that needs to be done in that area.

All things considered the past year was a very rewarding time for us, and we are in good hope that during this year we can finish the build-up and get started on some exciting new physics.

Appendix A

Relevant transitions of ^{6}Li

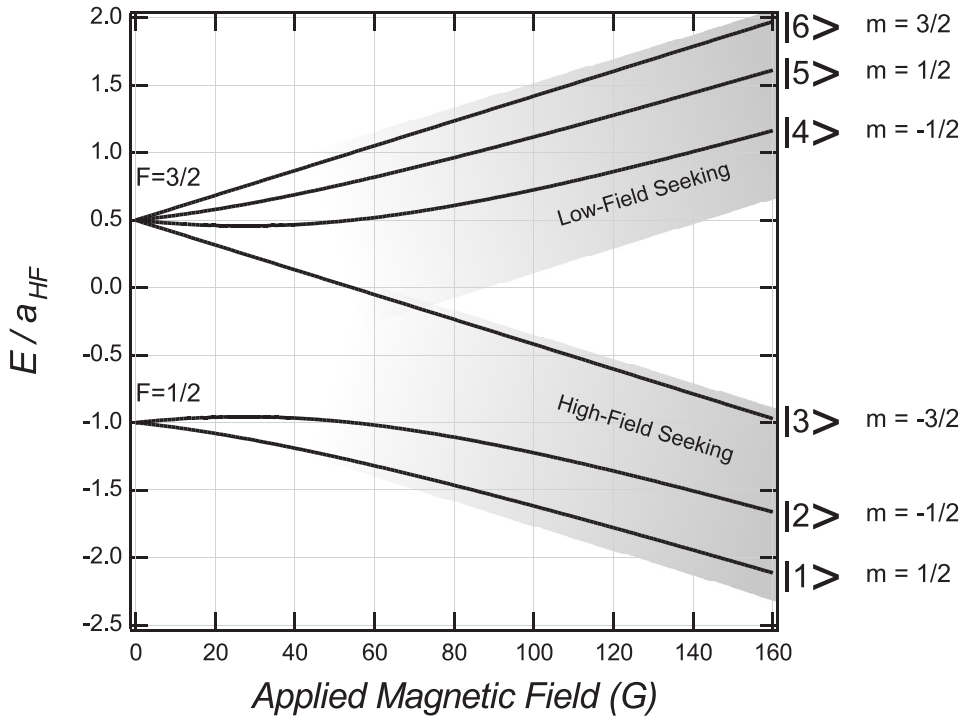

Figure A.1: Ground state hyperfine structure of ^{6}Li. Figure taken from [28]

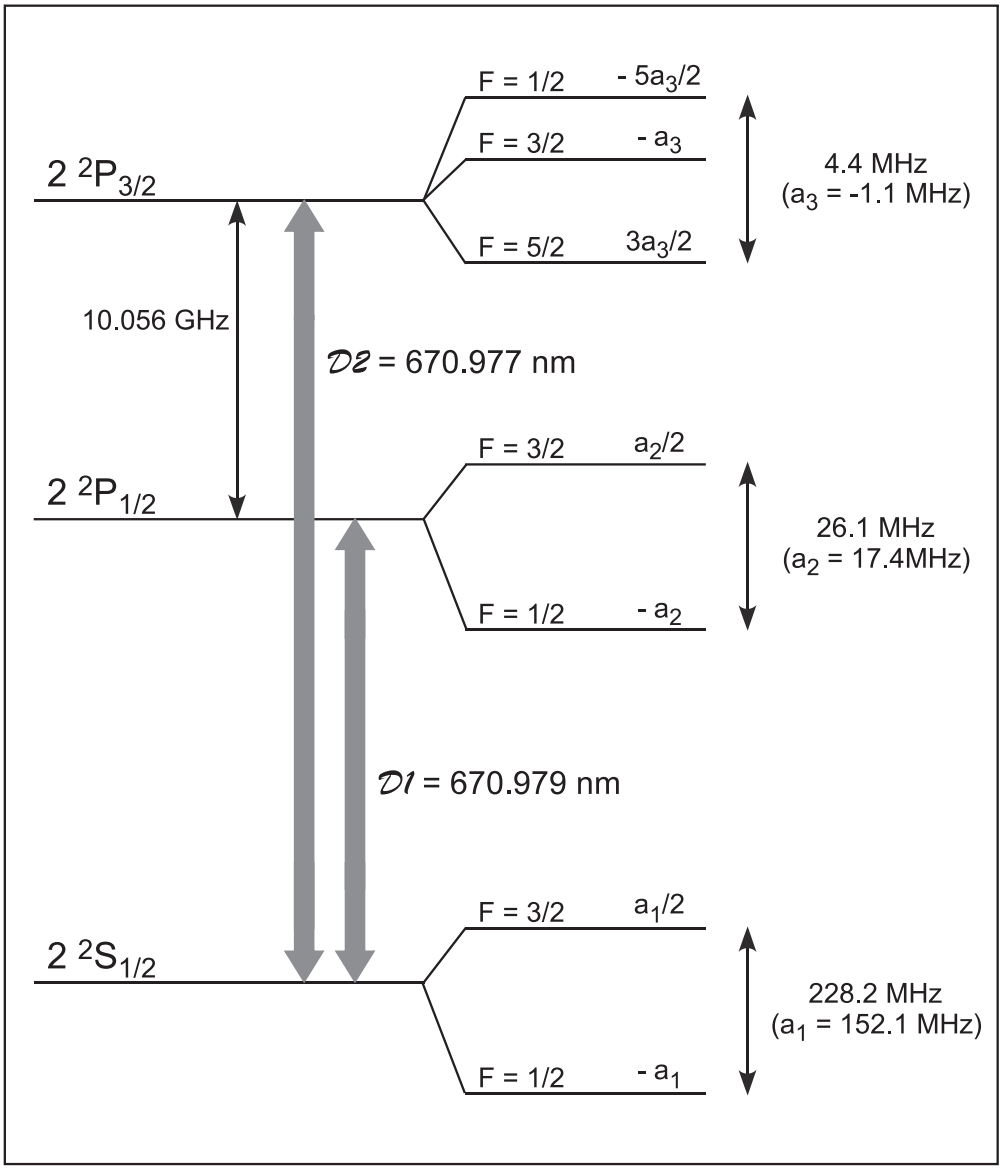

Figure A.2: Level scheme of ^{6}Li. Figure taken from [28]

Bibliography

[1] M. H. Anderson, J. R. Ensher, M. R. Matthews, C. E. Wieman, and E. A. Cornell. Observation of Bose-Einstein condensation in a dilute atomic vapor. *Science*, 269:198, 1995.

[2] K. B. Davis, M. O. Mewes, M. R. Andrews, N. J. van Druten, D. S. Durfee, D. M. Kurn, and W. Ketterle. Bose-Einstein condensation in a gas of sodium atoms. *Phys. Rev. Lett.*, 75(22):3969–3973, Nov 1995.

[3] C. C. Bradley, C. A. Sackett, J. J. Tollett, and R. G. Hulet. Evidence of Bose-Einstein condensation in an atomic gas with attractive interactions. *Phys. Rev. Lett.*, 75(9):1687–1690, Aug 1995.

[4] S. Inouye, M. R. Andrews, J. Stenger, H.-J. Miesner, D. M. Stamper-Kurn, and W. Ketterle. Observation of Feshbach resonances in a Bose-Einstein condensate. *Nature*, 392:151, 1998.

[5] B. DeMarco and D. S. Jin. Onset of fermi degeneracy in a trapped atomic gas. *Science*, 285(5434):1703–1706, 1999.

[6] J. Bardeen, L. N. Cooper, and J. R. Schrieffer. Microscopic theory of superconductivity. *Phys. Rev.*, 106(1):162–164, Apr 1957.

[7] S. Jochim, M. Bartenstein, A. Altmeyer, G. Hendl, S. Riedl, C. Chin, J. Hecker Denschlag, and R. Grimm. Bose-einstein Condensation of molecules. *Science*, 302:2101, 2003.

[8] M Greiner, C. A. Regal, and D. S. Jin. Emergence of a molecular Bose-Einstein condensate from a Fermi gas. *Nature*, Nov 2003.

[9] M. W. Zwierlein, C. A. Stan, C. H. Schunck, S. M. F. Raupach, S. Gupta, Z. Hadzibabic, and W. Ketterle. Observation of Bose-Einstein condensation of molecules. *Phys. Rev. Lett.*, 91(25):250401, Dec 2003.

[10] Friedhelm SerWane. The setup of a magneto optical trap for the preperation of a mesoscopic degenerate Fermi gas. Diploma thesis, 2007.

[11] Harold J. Metcalf and Peter van der Straten. *Laser Cooling and Trapping*. Springer-Verlag, New York, 1999.

[12] R. Grimm, M. Weidemüller, and Y. B. Ovchinnikov. Optical dipole traps for neutral atoms. *Molecular and Optical Physics*, 42:95, 2000.

[13] Thorsten Fießbach. *Quantenmechanik*. Spektrum Akademischer Verlag, 2005.

[14] J. J. Sakurai. *Modern Quantum Mechanics*. Addison-Wesley, 1994.

[15] Selim Jochim. *Bose-Einstein Condensation of Molecules*. PhD thesis, Universität Innsbruck, 2004.

[16] Martin Zwierlein. *High-Temperature Superfluidity in an Ultracold Fermi Gas*. PhD thesis, MIT, 2006.

[17] M. Bartenstein, A. Altmeyer, S. Riedl, R. Geursen, S. Jochim, C. Chin, J. Hecker Denschlag, R. Grimm, A. Simoni, E. Tiesinga, C. J. Williams, and P. S. Julienne. Precise determination of ^{6}Li cold collision parameters by radio-frequency spectroscopy on weakly bound molecules. *Physical Review Letters*, 94(10):103201, 2005.

[18] D. S. Petrov, C. Salomon, and G. V. Shlyapnikov. Weakly bound dimers of fermionic atoms. *Phys. Rev. Lett.*, 93(9):090404, Aug 2004.

[19] C. Chin and R. Grimm. Thermal equilibrium and efficient evaporation of an ultracold atom-molecule mixture. *Phys. Rev. A*, 69(3):033612, Mar 2004.

[20] K. M. O'Hara, M. E. Gehm, S. R. Granade, and J. E. Thomas. Scaling laws for evaporative cooling in time-dependent optical traps. *Phys. Rev. A*, 64(5):051403, Oct 2001.

[21] L. Luo, B. Clancy, J. Joseph, J. Kinast, A. Turlapov, and J.E. Thomas. Evaporative cooling of unitary Fermi gas mixtures in optical traps. *New Journal of Physics*, 8(9):213, 2006.

[22] D. S. Petrov, C. Salomon, and G. V. Shlyapnikov. Scattering properties of weakly bound dimers of fermionic atoms. *Physical Review A (Atomic, Molecular, and Optical Physics)*, 71(1):012708, 2005.

[23] C. J. Pethick and H. Smith. *Bose-Einstein-Condensation in Dilute Gases*. Cambridge University Press, 2002.

[24] U. Schunemann, H. Engler, R. Grimm, M. Weidemuller, and M. Zielonkowski. Simple scheme for tunable frequency offset locking of two lasers. *Review of Scientific Instruments*, 70(1):242–243, 1999.

[25] Jonas Fölling. Bose-Einstein Josephson tunnelling and generation of arbitrary optical potentials. Diploma thesis, 2005.

[26] S. Jochim, M. Bartenstein, G. Hendl, J. Hecker Denschlag, R. Grimm, A. Mosk, and M. Weidemüller. Magnetic field control of elastic scattering in a cold gas of fermionic lithium atoms. *Phys. Rev. Lett.*, 89(27):273202, Dec 2002.

[27] C. H. Schunck, M. W. Zwierlein, C. A. Stan, S. M. F. Raupach, W. Ketterle, A. Simoni, E. Tiesinga, C. J. Williams, and P. S. Julienne. Feshbach resonances in fermionic ^{6}Li. *Physical Review A (Atomic, Molecular, and Optical Physics)*, 71(4):045601, 2005.

[28] M. E. Gehm. Properties of $^6\mathrm{Lithium}$, 2003: *http://www.phy.duke.edu/research/photon/qoptics/techdocs/pdf/PropertiesOfLi.pdf*.

Acknowledgements

There are a lot of people who helped me complete this thesis, and I can thank only a fraction of them here.

The first ones I would like to thank are the members of my family, especially my father, who began to explain the world to me as soon as I was old enough to listen, starting me on the road that would lead to physics.

To Friedhelm, Timo and Matthias I owe thanks for many things. First of all the relaxed and friendly atmosphere we all work in, which is in no small part due to their patience towards my many flaws. When I joined up Friedhelm and Timo made me feel welcome at once, and were always patient with me when I asked for their advice. I am glad that I will be able to spend at least a part of the next three years with you.

With my thesis due in five weeks, no dipole trap, untested Feshbach coils, a dismantled MOT and of course without any mesurements I could use for my thesis, they made an incredible effort in the final week before the christmas holidays, which left us with a dipole trap containing $3 \cdot 10^6$ atoms, working Feshbach coils and absorption imaging, ready to begin evaporative cooling. Without this effort of the whole group chapter four of this thesis would look very different.

To the members of the group of professor Ullrich I am grateful for helping out whenever we needed equipment or advice, for being there when we needed adversaries at the soccer table, and for tolerating our messing around with black sludge in their chemichal laboratory (It will be over soon, we promise!).

The mechanical workshop did a lot of work for us during this year, for which we are grateful. But my special thanks go to Florian Säubert and Stephan Flicker, the supervisors of the teaching workshop. We could walk into their office with a problem and a vague idea of what might be done about it, and usually left knowing we would hold the solution in our hands a few days later.

André I thank for lending us his skills with a razor blade, which got me out of a rather unusual predicament, and Gerhard and Valentin for not only progamming the digital PID controllers, but also integrating them smoothly into our Labview interface, this will make our life in the lab a lot easier.

And of course there is Selim, with his is knowledge, experience and unbelievable dedication towards his students. He was always willing to explain things a second (or third) time, responded to my embarrassed reports of the acts of destruction and stupid mistakes I committed in the lab with a calm 'these things happen...' and, in the final weeks before my thesis was due, spent his nights in the lab with me, trying to get the dipole trap to work. He is a better supervisor than I could have ever hoped for.

Erklärung:

Ich versichere, dass ich diese Arbeit selbstständig verfasst und keine anderen als die angegebenen Quellen und Hilfsmittel benutzt habe.

Heidelberg, den _____ _____

Unterschrift